CHAPTER-3

Synthesis, characterization, and electrocatalytic performance of magnesium doped bismuth copper titanate (BCTO) for oxygen evolution reaction

3.1. Abstract

Designing high-efficiency electrocatalysts for water oxidation has become increasingly important in the catalysis field owing to its implications for renewable energy production and storage. The production of hydrogen (H_2) from water is hampered by the very sluggish kinetics of the water-splitting process. Enhancement of effective oxygen evolution reaction (OER) electrocatalysts is also required to understand the primary barrier to OER. This article investigates the electrochemical activity of magnesium-doped bismuth copper titanate (Mg-BCTO) as an efficient catalyst for the OER in water electrolysis, a critical step in hydrogen production for sustainable energy. The synthesized materials, including various stoichiometries of Mg-doped BCTO, undergo thorough physical and electrochemical characterizations using XRD, FT-IR, Raman, FE-SEM, HR-TEM, XPS, CV, LSV, EIS, and Tafel polarization analyses. Remarkably, Mg0.1 doped BCTO demonstrates superior performance, achieving a current density of 10 mA cm^{-2} at a very low overpotential (η_{10}) of 265 mV and with a Tafel slope of 92 mV dec^{-1}. This finding not only highlights the electrocatalytic efficiency of Mg doped BCTO but also positions it as a promising model for the development of highly active and stable water oxidizing catalysts, contributing to the advancement of clean energy technologies.

3.2. Introduction

The search for alternative energy sources has become more important in the 21st century owing to a number of interrelated issues. First off, there are worries over the diminishing reserves of fossil fuels due to their limited supply, which might run out by the middle of this century, according to forecasts [1]. Furthermore, the necessity of reducing CO_2 emissions in order to

lessen the negative consequences of climate change has highlighted the need for sustainable and renewable energy alternatives. Photocatalytic water splitting, which uses solar energy to make clean hydrogen, is one potential path in this search for clean energy [2,3]. Since hydrogen is a fuel that is both ecologically benign and adaptable, this approach holds a lot of promise. Furthermore, there is no environmental harm caused by the oxygen that is created as a consequence of water splitting [4,5]. However, reducing the amount of electrical energy used during the process is crucial if water splitting is to be an economically feasible method to generate electricity [6]. Effective electrocatalysts are thus needed to support the various reactions involved in water splitting, especially the OER, which is a crucial stage in the procedure [7].

Due to the strong OER activity, metal oxide-based electrocatalysts like RuO_x and IrO_x have classically been preferred [8]. Nevertheless, the high cost of these materials prevents their widespread use. Consequently, research on more affordable alternative electrocatalysts having activity that is at par with or even better than current ones is ongoing. The family of materials known as perovskite-based electrocatalysts has demonstrated potential in this aspect [9–11]. Perovskite compounds have proven to be catalytically very active in a variety of applications and display a wide range of characteristics. However, issues including sluggish reaction kinetics and poor stability under extreme pH conditions prevent their utilization in OER [12]. Despite these obstacles, researchers are looking at material changes and optimization techniques to improve the performance of perovskite-based electrocatalysts for OER.

Multimetallic compounds such as $CaCu_3Ti_4O_{12}$ (CCTO), a typical $ACu_3Ti_4O_{12}$ (ACTO, where A = Sr, $Na_{1/2}Bi_{1/2}$ or $Na_{1/2}Y_{1/2}$, $Na_{1/2}La_{1/2}$, $Bi_{2/3}$, $Y_{2/3}$, $La_{2/3}$, Cd, Ca) have drawn interest among the materials under investigation because of their exceptional dielectric

characteristics and thermal stability [13]. These materials have been extensively studied for other applications, but their potential for OER remains relatively unexplored. Similarly, $Bi_{2/3}Cu_3Ti_4O_{12}$ (BCTO) has been discovered as a possible OER catalytic candidate due to its structural similarity with CCTO. However, its electrocatalytic properties for this particular application are still in the early stages.

To address this gap, we have used sophisticated method such as the semi-wet approach to synthesize BCTO and Mg doped variants $Bi_{2/3}Cu_{3-x}Mg_xTi_4O_{12}$ (where x = 0, 0.05, 0.1, 0.2) [13]. To thoroughly examine the structure and morphology of these materials, we have used a variety of characterization techniques, including energy dispersive spectroscopy (EDS), field emission scanning electron microscopy (FE-SEM), X-ray diffraction (XRD), Fourier transform infrared spectroscopy (FT-IR), Raman Spectroscopy, and transmission electron microscopy (TEM). Additionally, a thorough assessment of the electrocatalytic activity of BCTO and Mg doped BCTO for OER has been conducted in an alkaline electrolyte solution having 1.0 M KOH. Compared to other variants, Mg0.1 doped BCTO ($Mg_{0.1}$BCTO) has demonstrated considerably lower overpotential, indicating particularly promising OER activity among the investigated materials.

Thus, our work contributes to the development of sustainable energy technologies by advancing the development of effective and affordable electrocatalysts for OER. To completely comprehend the underlying principles and maximize the performance of these materials for practical application in hydrogen generation and other areas, more research is necessary.

3.3. Experimental

3.3.1. Materials

Copper acetate $Cu(CH_3COO)_2 \cdot H_2O$ (99 % Merck, India), bismuth nitrate $Bi(NO_3)_3 \cdot 5H_2O$ (purity around 98 % Merck, India), titanium oxide TiO_2 (purity around 98.5 % Merck, India), citric acid (99.5 % Merck, India), magnesium acetate $Mg(CH_3COO)_2 \cdot H_2O$ (purity around 98.5 % Merck, India).

3.3.2. Synthesis of BCTO and Mg doped BCTO

A semi-wet technique was used to synthesize $Bi_{2/3}Cu_{3-x}Mg_xTi_4O_{12}$ (where x = 0, 0.05, 0.1, and 0.2) from a previously reported literature [13], which are termed as BCTO, $Mg_{0.05}$BCTO, $Mg_{0.1}$BCTO, and $Mg_{0.2}$BCTO for x = 0, 0.05, 0.1, and 0.2, respectively. The stoichiometric ratios of copper acetate, magnesium acetate, titanium oxide, and bismuth nitrate were used in this method. For this, a solution of copper acetate, magnesium acetate, and bismuth nitrate was mixed in distilled water, afterwards, it was combined with solid TiO_2. A suitable quantity of citric acid, that acts as a fuel, was made soluble in distilled water, and then incorporated into the mixture. A hotplate was used to heat the resulting solution to a temperature range of 343 to 353 K in order to remove moisture. BCTO and Mg-doped BCTO powders having fluffy mass were formed when the gasses were removed.

3.3.3. Preparation of working electrode

The FTO (fluorine-doped tin oxide) substrate was cut into 1×1 cm^2 pieces and cleaned using ethanol, acetone, and water in that order. To create a hydrophilic surface, ultrasonication was done for about an hour during the cleaning process. In order to prepare the catalyst ink, 1 mg

of the prepared catalysts, was dissolved in a mixture of 40 µL ethyl alcohol, 20 µL double distilled water, and 10 µL of 5 % nafion solution used as a binder. After that, the mixture was ultrasonically treated for about an hour. After that, 20 µL of the resultant ink, was drop casted onto the FTO substrate and allowed to air dry at ambient temperature. After applying the catalyst ink coating, the FTO plates were dried in an oven at 373 K for a few hours, to be used as working electrodes in the studies that followed.

3.4. Characterizations

3.4.1. Physicochemical Characterizations

Using a diffractometer (Rigaku Smart Lab 9 kW), powder X-ray diffraction (XRD) at a wavelength of 1.514 Å, was used to examine the crystalline nature of the prepared samples. The FTIR spectra of prepared catalysts was characterized by ATR-FTIR (Bruker, ALPHA model) Spectrophotometer in the frequency range 500–1500 cm^{-1}. A Raman spectrometer (α-300, AFM SNOM) was used to record the Raman spectra. Using transmission electron microscopy (TEM) on a Thermo Fisher Technai 20 G^2 and field emission scanning electron microscopy (FE-SEM) on a Nova Nano-SEM, the morphologies and microstructures of the materials were investigated. X-ray photoelectron spectroscopy (XPS) investigation was conducted using K-alpha XPS device.

3.4.2. Electrochemical Characterizations

The electrochemical studies were conducted with a three-electrode system within a single compartment glass cell made up of Pyrex. The setup comprised a circular platinum (Pt) foil with an area of 8 cm^2, obtained from Aldrich with a purity of 99.9 %, serving as the counter electrode, coated FTO (fluorine-doped tin oxide) plates with a 0.50 cm^2 area acting as the

working electrode and a reference electrode utilizing Hg/HgO in a solution of 1 M KOH. The electrochemical cell was cleaned before use by first boiling it in a 1:3 mixture of H_2SO_4 and HNO_3, then heating it in ultrapure water. The cell was then repeatedly rinsed with ultrapure water, followed by acetone, and finally dried in an oven at 80 ^oC for 30 to 40 minutes. Pt wire was then immersed in a 20 % HNO_3 solution for a short while after being cleaned with pure water, and FTO was ultrasonically cleaned using ethanol, soap solution, and water in that order to produce a hydrophilic surface. To bridge the electrolyte in the cell with the reference electrode, a luggin capillary salt bridge was established. This bridge was made with KCl and agar-agar. All recorded potentials in this investigation, were referenced to the Hg/HgO/1 M KOH reference electrode, with a standard potential ($E^0_{Hg/HgO}$) of 105.3 mV vs. the normal hydrogen electrode (NHE) [14]. The electrochemical characterizations were conducted using a CHI-608 C instrument manufactured by CH Instruments, USA. Various electrochemical techniques were employed, including cyclic voltammetry (CV), impedance measurements (EIS), and Tafel polarization investigations. These techniques were employed following established methodologies as referenced in prior studies [15,16].

As per **Equation 3.1**, all potentials measured with the Hg/HgO reference electrode were transformed to correspond with the reversible hydrogen electrode (RHE).

$$E_{RHE} = E^0_{Hg/HgO} + E_{Hg/HgO} + 0.0592 \times pH \qquad \textbf{(3.1)}$$

3.5. Results and discussion

3.5.1. Physicochemical Characterizations

3.5.1.1. XRD

The X-ray diffraction pattern depicted in **Figure 3.1** illustrates the presence of BCTO phase (identified by JCPDS card no. 46-0725) in both Mg-doped and undoped BCTO samples, where the peaks corresponding to (2 0 0), (2 1 1), (2 2 0), (3 1 0), (2 2 2), (3 2 1), (4 0 0), (4 2 2), and (4 4 0) planes align closely with those of CCTO (JCPDS card no. 75-2188). The small peak around (211) plane is the secondary phase of rutile TiO_2 (JCPDS card no. 21-1276), which is present in trace amounts in all the samples. These patterns closely resemble those that have already been documented [13,17]. By employing the Debye–Scherrer's formula (**Equation 3.2**), the crystallite size (D) of the synthesized samples were determined [18].

$$D = \frac{k\lambda}{\beta \cos\theta} \qquad \textbf{(3.2)}$$

The diffraction angle is indicated by θ, the full-width half maximum (FWHM) is shown by β, and the XRD wavelength is represented by λ. The crystal shape coefficient (k) is fixed at 0.89 [19]. BCTO, $Mg_{0.05}$BCTO, $Mg_{0.1}$BCTO, and $Mg_{0.2}$BCTO ceramics were found to have average crystallite diameters of 34.97 nm, 43.96 nm, 47.08 nm, and 45.02 nm, respectively.

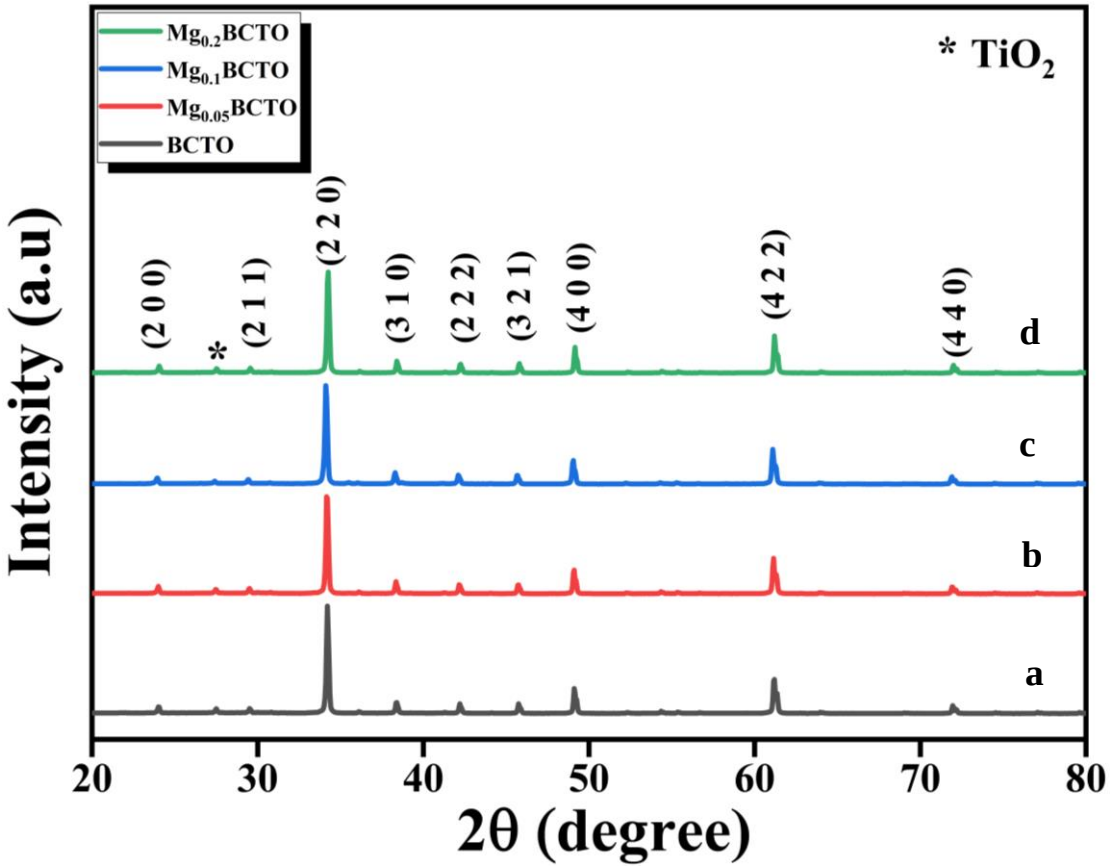

Figure 3.1. XRD patterns of **a)** BCTO, **b)** $Mg_{0.05}$BCTO, **c)** $Mg_{0.1}$BCTO and **d)** $Mg_{0.2}$BCTO catalysts.

3.5.1.2. FTIR

Figure 3.2 displays the FT-IR spectra of the BCTO and Mg doped BCTO ceramic materials, highlighting specific peaks that elucidate the material's composition and bonding properties. A tiny absorption peak at 547 cm^{-1} is ascribed to the bending mode of copper oxide (CuO) [20]. The band recorded at 594 cm^{-1} specifically corresponds to Ti–O stretching vibration. This band signify the formation of perovskite phase of the bismuth copper titanate ceramic [21,22].The absorption band at 743 cm^{-1} is linked to a Bi–O metal oxide bond, indicating the presence of bismuth oxide in the structure [23]. The bands observed at 1098 cm^{-1} is ascribed to the C-N bond stretching [24].

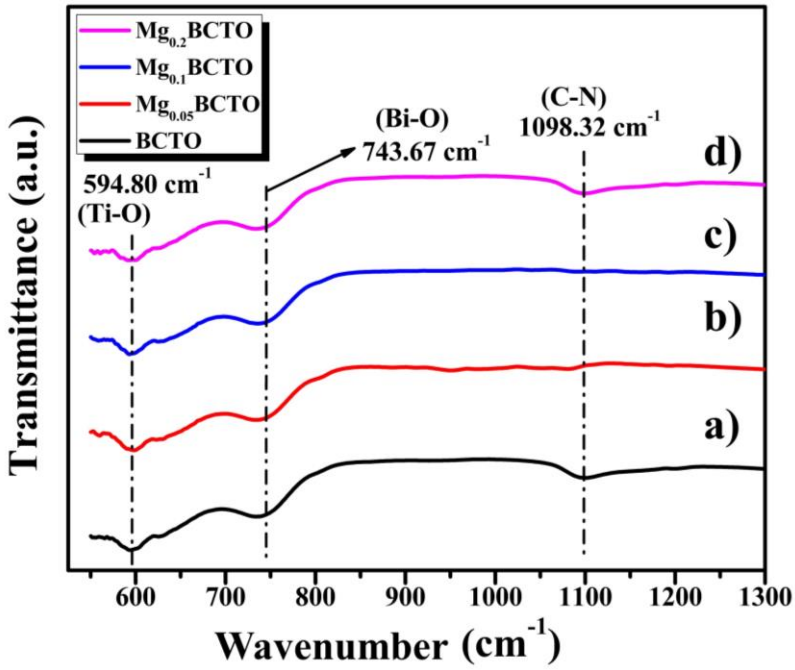

Figure 3.2. FT-IR spectra of **a)** BCTO, **b)** $Mg_{0.05}$BCTO, **c)** $Mg_{0.1}$BCTO, **d)** $Mg_{0.2}$BCTO catalysts.

3.5.1.3. Raman Spectroscopy

Figure 3.3 illustrates the Raman spectrum of $Bi_{2/3}Cu_{3-x}Mg_xTi_4O_{12}$ for x value of 0.1 recorded in the range of 200–1000 cm^{-1}. The spectra reveal multiple modes at 263, 432, 511, 606, and 708 cm^{-1}. The modes observed at 432 and 511 cm^{-1}, associated with A_g symmetry, suggest the rotational movement of TiO_6 (octahedron) and the related anti-stretching vibrations of the Ti–O–Ti bonds [25,26]. The presence of the modes at 432, and 511 cm^{-1} confirms the phase of bismuth titanate in the synthesized catalysts [27].

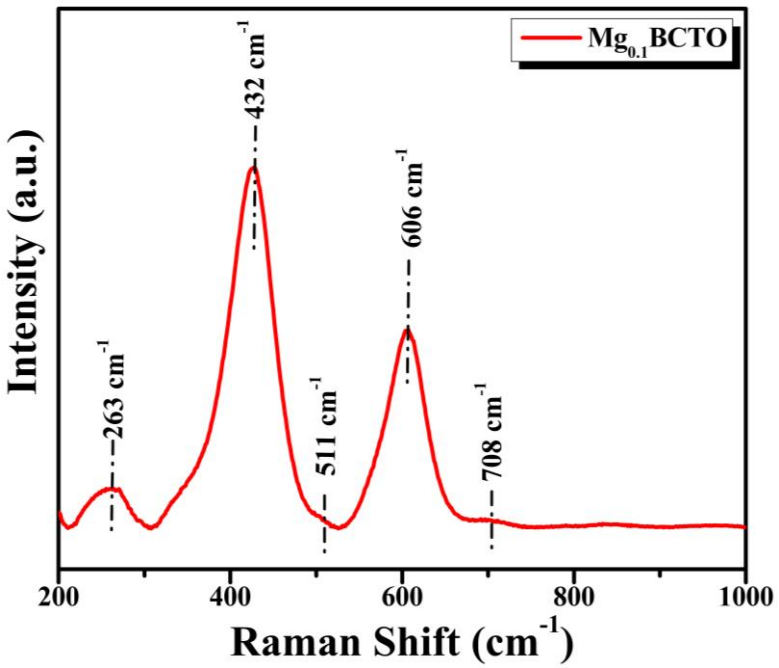

Figure 3.3. Raman spectrum of $Mg_{0.1}$BCTO.

According to lattice dynamic calculations (LCD), the mode associated with stretching vibration of Ti–O–Ti typically appears at 708 cm^{-1} [28]. Nevertheless, as stated by C. Mu *et al.*, this mode can shift to higher wavenumbers [29]. The weakest mode was observed around 263 cm^{-1} may indicate the presence of a CuO phase, which contrasts with the XRD results, where no phases other than the bismuth copper titanate phase were detected. Such low-frequency vibrations in perovskite oxides are often associated with the relative motion of Bi–O and Ti–O sublattices. These modes can be interpreted in terms of longitudinal optical (LO) and transverse optical (TO) phonon splitting, which originates from long-range Coulomb interactions in polar crystals. The presence of both LO and TO contributions reflects the anisotropic nature of lattice vibrations and is commonly observed in ferroelectric and perovskite systems. Incorporating this interpretation strengthens the assignment of the observed bands, highlighting that the 263 cm^{-1} peak is not an artifact but an intrinsic vibrational

mode of the Mg-BCTO structure. This detailed understanding further supports the structural integrity of the lattice and demonstrates that doping does not suppress the fundamental phonon activity of the bismuth titanate phase. This discrepancy arises because Raman spectroscopy is more sensitive than XRD, making it capable of detecting phases that XRD could not [27]. Raman spectra of other stoichiometries are shown in the following **Figure 3.4**.

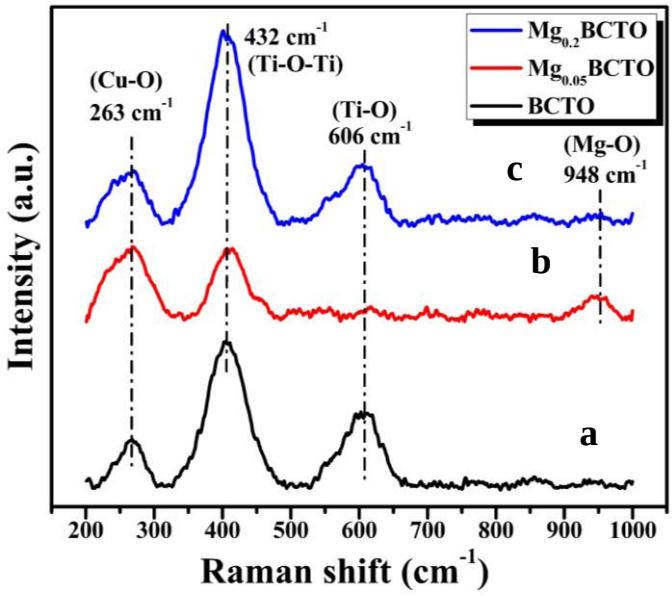

Figure 3.4. Raman spectra of **a)** BCTO, **b)** $Mg_{0.05}$BCTO, **c)** $Mg_{0.2}$BCTO.

3.5.1.4. FE-SEM

The field emission scanning electron microscopy (FE-SEM) images for the $Bi_{2/3}Cu_{3-x}Mg_xTi_4O_{12}$ (Mg doped BCTO) particles with x = 0.1 are shown in **Figures 3.5 (a) and (b)**. The micrographs show that most of the particles have forms that resemble cubes, yet there is a discernible variance in the sizes of the particles among the samples, which is a feature common to the BCTO structure [27,30,31]. As shown in **Figure 3.5 (f)**, the average particle size for the composition with x = 0.1 is found to be around 0.35 μm [13].

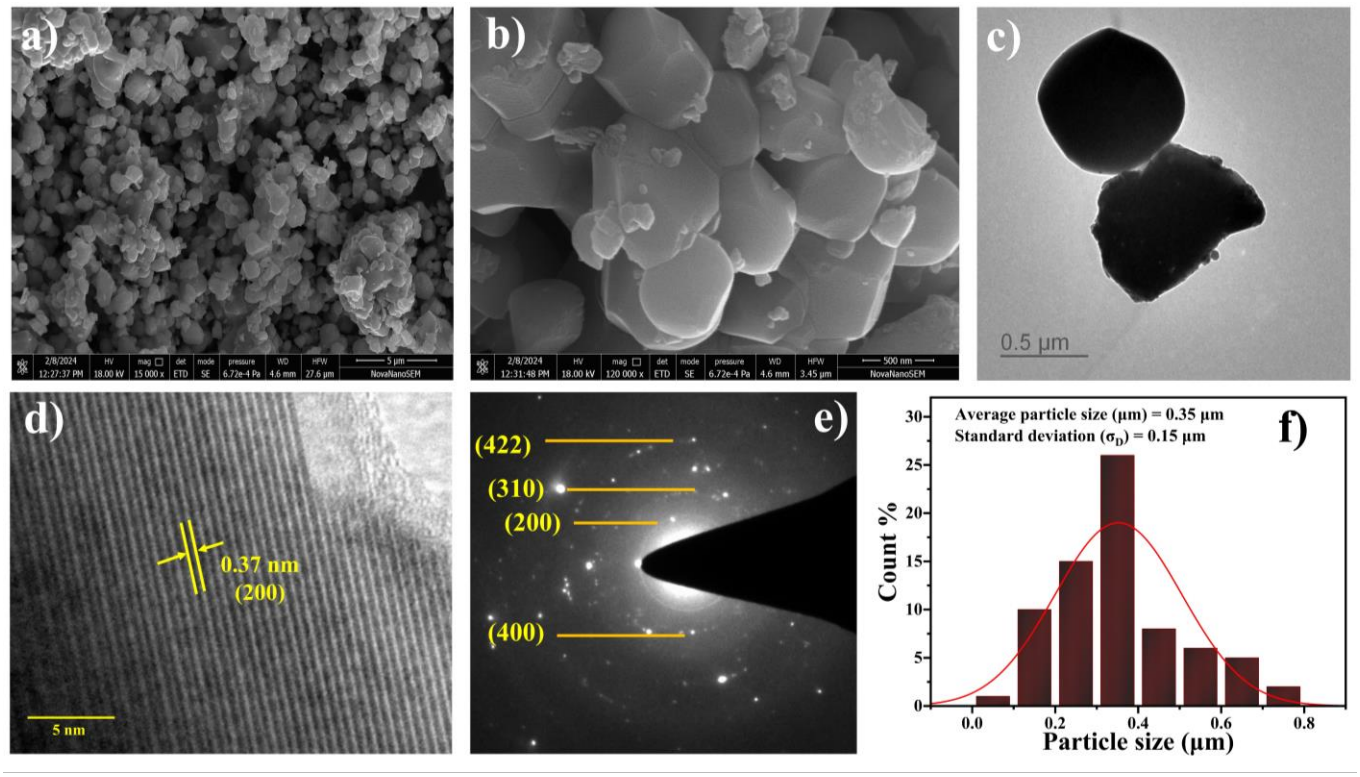

Figure 3.5. a, b) SEM images of $Mg_{0.1}$BCTO at different magnifications, **c)** TEM image of $Mg_{0.1}$BCTO, **d)** HR-TEM image of $Mg_{0.1}$BCTO, **e)** SAED pattern, **f)** Particle size distribution of $Mg_{0.1}$BCTO with standard deviation.

Figure 3.6 and **Figure 3.7** illustrates the use of EDS and elemental mapping to further examine the constituent distribution and composition of Mg doped BCTO particles. All the anticipated elements, i.e., Bi, Cu, Mg, Ti, and O are present in the sample for x = 0.1. This thorough examination confirms that the specified stoichiometric ratios were reached with the introduction of trace amounts of TiO_2 and CuO. It also shows that the host and replaced elements are equally distributed across the sample. Additionally, FE-SEM images **(Figure 3.8)**, EDS spectra and elemental mapping **(Figure 3.9 and Figure 3.10)** of BCTO and other Mg doped BCTO stoichiometries are provided for comparison.

The SEM micrographs **(Figure 3.8)** reveal distinct morphological differences between undoped and Mg-doped BCTO ceramics. The undoped sample **(Figure 3.8 (a))** shows mostly unfaceted grains with irregular outlines, whereas the Mg-doped samples exhibit more prominently faceted grains with well-defined crystal faces. Interestingly, faceted structures are visible even in the undoped material despite the relatively low-temperature processing conditions, suggesting an inherent tendency toward anisotropic growth. However, the degree of faceting is enhanced in the Mg-doped samples, indicating that Mg incorporation promotes anisotropy and preferential growth along specific crystallographic planes. In addition to faceting, a noticeable reduction in average grain size is observed with increasing Mg content, suggesting that Mg doping simultaneously inhibits grain growth while promoting more ordered, anisotropic morphology.

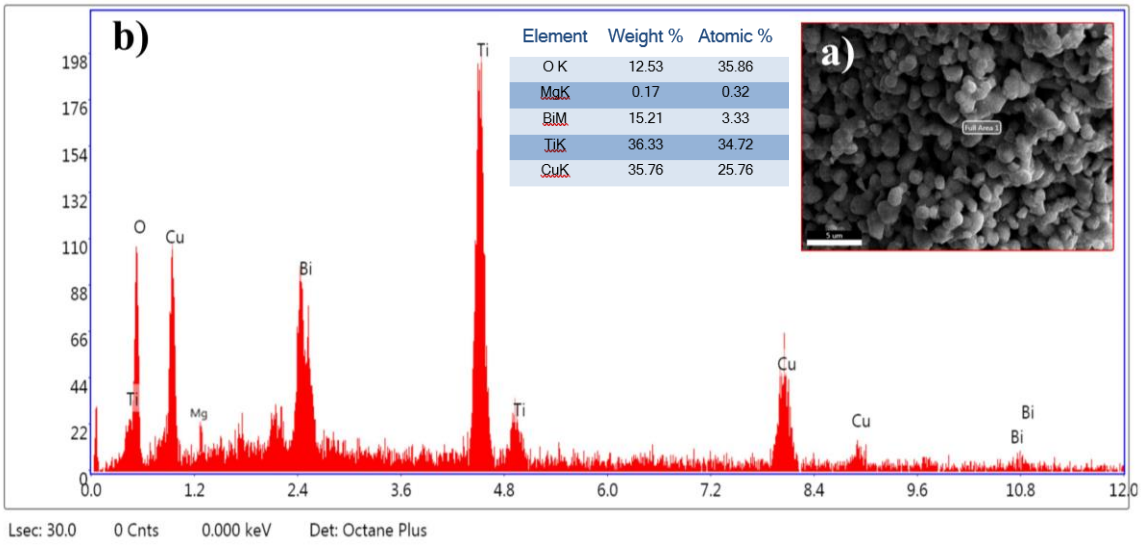

Figure 3.6. a) FE-SEM image of $Mg_{0.1}$BCTO, **b)** Corresponding EDS spectra.

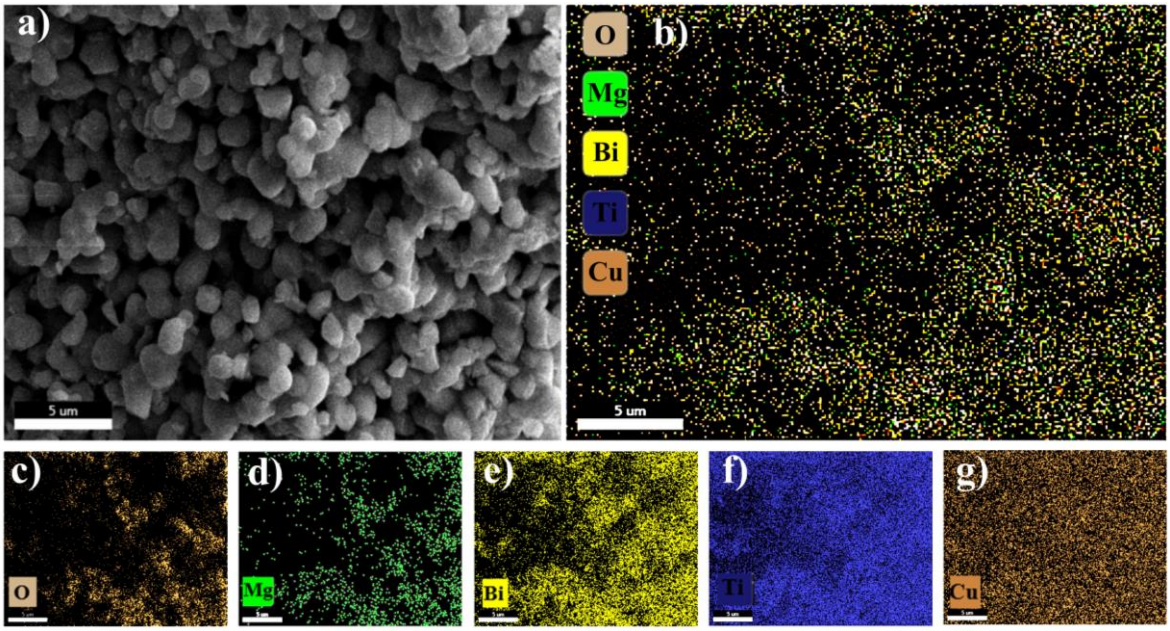

Figure 3.7. Elemental mapping of $Mg_{0.1}$BCTO.

3.5.1.5. HR-TEM

The transmission electron microscopy (TEM) technique was utilized to examine the detailed microstructure of the Mg doped BCTO ($Mg_{0.1}$BCTO). In **Figure 3.5 (c)**, the TEM image reveals that the Mg doped BCTO particles possess cubical shape of crystalline particles aligning well with the observations from scanning electron microscopy (SEM) analysis. Due to particle agglomeration, some particles are found to be larger in size which is a common property of such materials [32]. Further, the HR-TEM image shown in **Figure 3.5 (d)**, reveals distinct lattice fringes with interplanar spacing of 0.37 nm. This spacing correspond to the (2 0 0) crystal plane of the $Mg_{0.1}$BCTO material. Moreover, the selected area electron diffraction (SAED) pattern depicted in **Figure 3.5 (e)**, taken from a specific region of the material, displays a combination of discrete dots and rings. This pattern is indicative of a material that exhibits polycrystalline characteristics [31]. These detailed TEM observations not only

corroborate the findings from SEM analysis but also reveal the intricate nature of the Mg doped BCTO material.

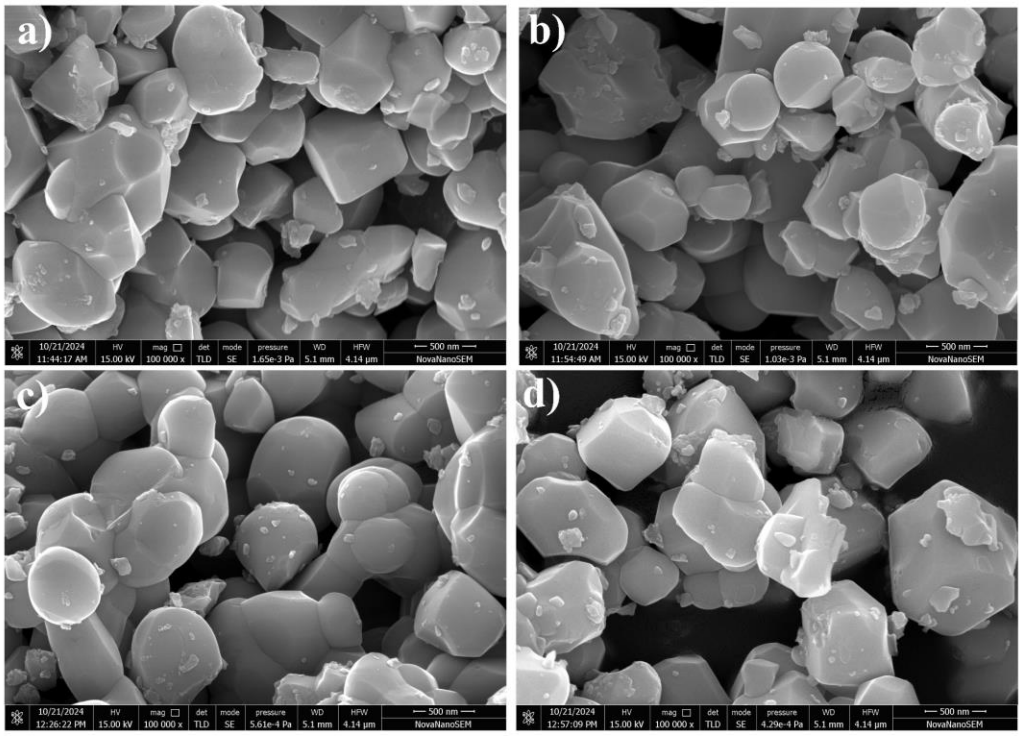

Figure 3.8. FE-SEM images of **a)** BCTO, **b)** $Mg_{0.05}$BCTO, **c)** $Mg_{0.1}$BCTO, **d)** $Mg_{0.2}$BCTO.

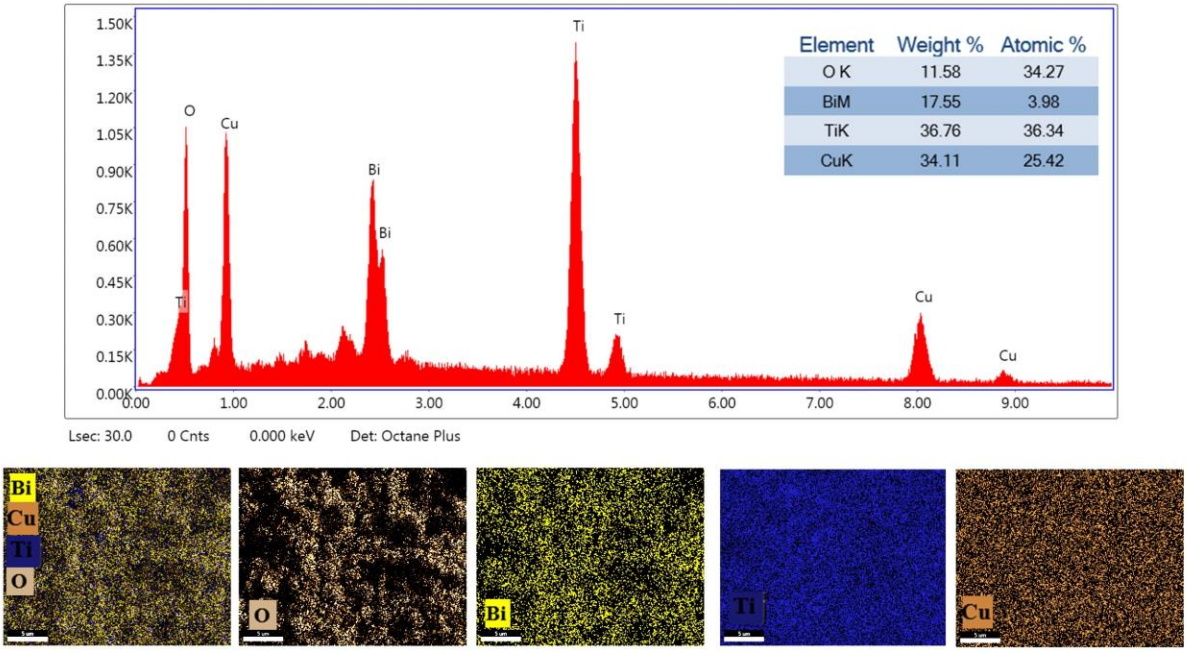

Figure 3.9. EDS spectra and elemental mapping of BCTO ceramic material.

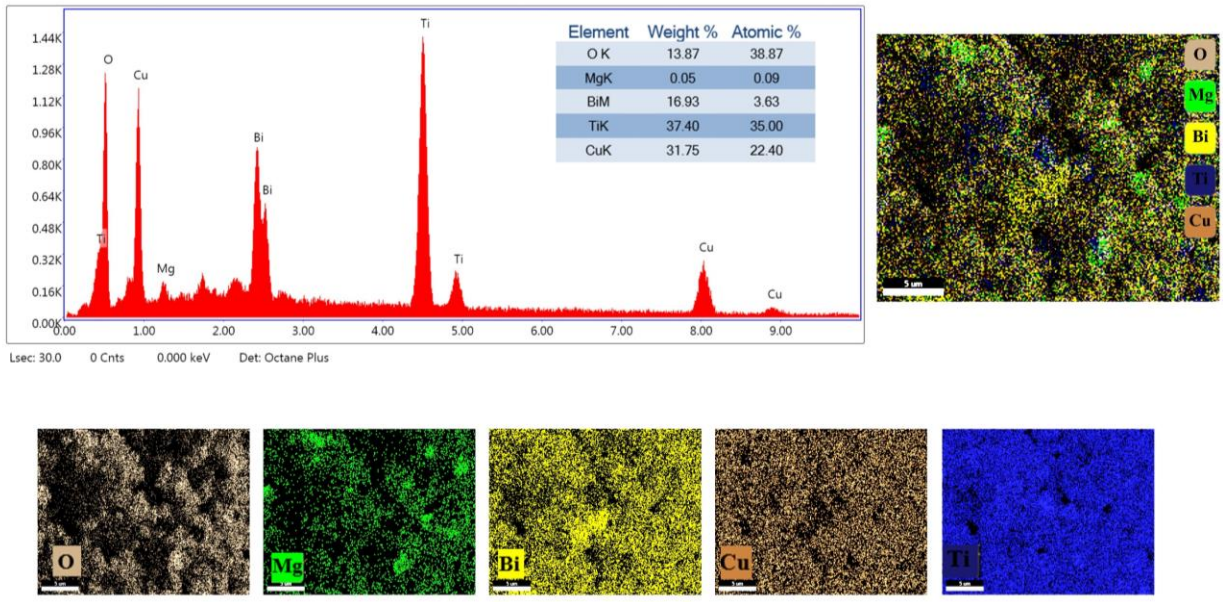

Figure 3.10. EDS spectra and elemental mapping of BCTO ceramic material.

3.5.1.6. XPS

The catalyst's ($Mg_{0.1}$BCTO) coordination environment and chemical state were analyzed using X-ray photoelectron spectroscopy (XPS). The spectra ascertain the constituents of the Mg doped BCTO, revealing the presence of Mg, Bi, Cu, Ti and O as shown in **Figure 3.11**. These results elucidate the binding states of the various constituents inside the catalyst. The high-resolution Mg 1s spectrum displays one distinct peak at binding energy of 1,303.5 eV. **Figure 3.11 (a)** represents the deconvolution of this peak. This observed peak is indicative of MgO, thereby affirming the existence of Mg ions in the +2 oxidation state within the ceramic material [33]. The Bi $4f_{5/2}$ and Bi $4f_{7/2}$ states are represented by two prominent and symmetrical peaks at 163.36 eV and 158.7 eV, respectively, in the high-resolution XPS spectra of the Bi 4f core level for the Mg doped BCTO sample [34]. The intrinsic spin-orbit coupling, which splits the Bi 4f core level into two sublevels, is the source of these peaks. This splitting is shown in **Figure 3.11 (b)**, which displays a thorough scan of the Bi 4f spectrum. The presence of the Bi element in its trivalent form (Bi^{3+}) is indicated by these binding energies [35]. **Figure 3.11 (c)** depicts the Cu 2p XPS spectrum of the $Mg_{0.1}$BCTO sample, where the peaks with binding energies of 933.2 eV and 953.1 eV correspond to the Cu $2p_{3/2}$ and Cu $2p_{1/2}$ states, respectively, showing the existence of +2 (Cu^{2+}) oxidation state of Cu. The appearance of satellite peaks at 943.7 eV and 963.1 eV further validates this [36,37]. The spin-orbit doublet of Ti, namely the Ti $2p_{3/2}$ and Ti $2p_{1/2}$ states, is represented by the two separate peaks seen at around 457.21 eV and 463.2 eV respectively **(Figure 3.11 (d))**. According to earlier reported research [38,39], these binding energies are in line with the existence of tetravalent Ti ions (Ti^{4+}) inside the TiO_2 lattice. On the spectrum's lower binding energy side, two different O^{2-} ion types were found **(Figure 3.11 (e))**. About 2.0 eV more binding energy can be seen for O_{vac} 1s peak than the O^{2-}

1s peak in M-O bond. Oxides that include cations in several valence states often exhibit this dual peak structure for O 1s [40]. It has been proposed that O^{2-} ions of M-O bond, are surrounded by a full complement of six nearest-neighbor O^{2-} ions, while O_{vac}^{2-} ions are located in oxygen-deficient regions [41]. In oxygen-deficient regions, the effective nuclear charge of an O_{vac}^{2-} 1s electron is higher relative to an O^{2-} 1s electron in M-O bond due to the reduced screening effect [40].

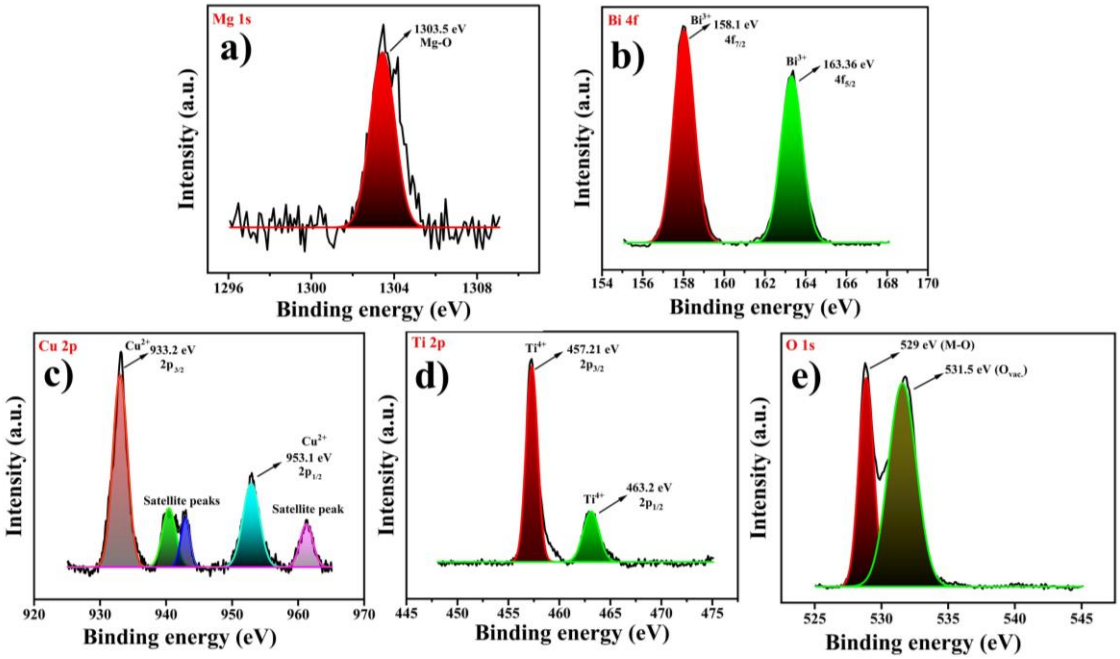

Figure 3.11. High resolution of XPS spectra of **a)** Mg 1s, **b)** Bi 4f, **c)** Cu 2p, **d)** Ti 2p, **e)** O1s.

3.5.2. Electrochemical characterizations

3.5.2.1. OER Study

The electrocatalytic activity of all the synthesized catalysts was assessed using linear sweep voltammetry (LSV) and electrochemical impedance spectroscopy (EIS). **Figure 3.12 (a)** displays the LSV, measured at a scan rate 0.5 mV s^{-1}, for BCTO and Mg doped BCTO. **Figure**

3.12 (a) demonstrates that the catalytic current rises as the Mg doping increases. Nevertheless, as the doping increases from $Mg_{0.1}$BCTO to $Mg_{0.2}$BCTO, a decline in catalytic activity was detected, most likely because of the structural morphology collapsing [42] or a decrease in oxygen vacancy formation [43]. Liu *et al.* discovered that the presence of oxygen vacancies has a substantial impact on boosting the performance of the OER. They observed that an increase in oxygen vacancies correlates with enhanced OER performance [44]. Oxygen vacancies provide an abundance of electrons, which enhance the attachment of adsorbates to the catalyst surface via interactions between the surface and the adsorbate [45,46]. In line with these findings, Mg doping has been reported to promote the generation of oxygen vacancies, which in turn improves the electronic conductivity of the system and contributes to the observed enhancement in OER activity. Thus, the superior activity of $Mg_{0.1}$BCTO can be attributed to an optimum balance between vacancy generation and structural stability, whereas excessive Mg incorporation ($Mg_{0.2}$BCTO) likely disrupts this balance, leading to reduced performance.

The overpotential for $Mg_{0.1}$BCTO was around 265 mV for achieving 10 mA cm^{-2} (η_{10}), which is the lowest and has the highest current density among all the prepared stoichiometries **(Figure 3.12 (c))** and almost equivalent to the overpotential of the state of the art catalyst RuO_2 (240 mV) [8]. In order to standardize the amount of material and roughness of the electrode on the substrate, the activity was also determined by calculating the current density per mg (specific current density) (**Equation 3.3**), and the true current density **(Equation 3.4)** [47].

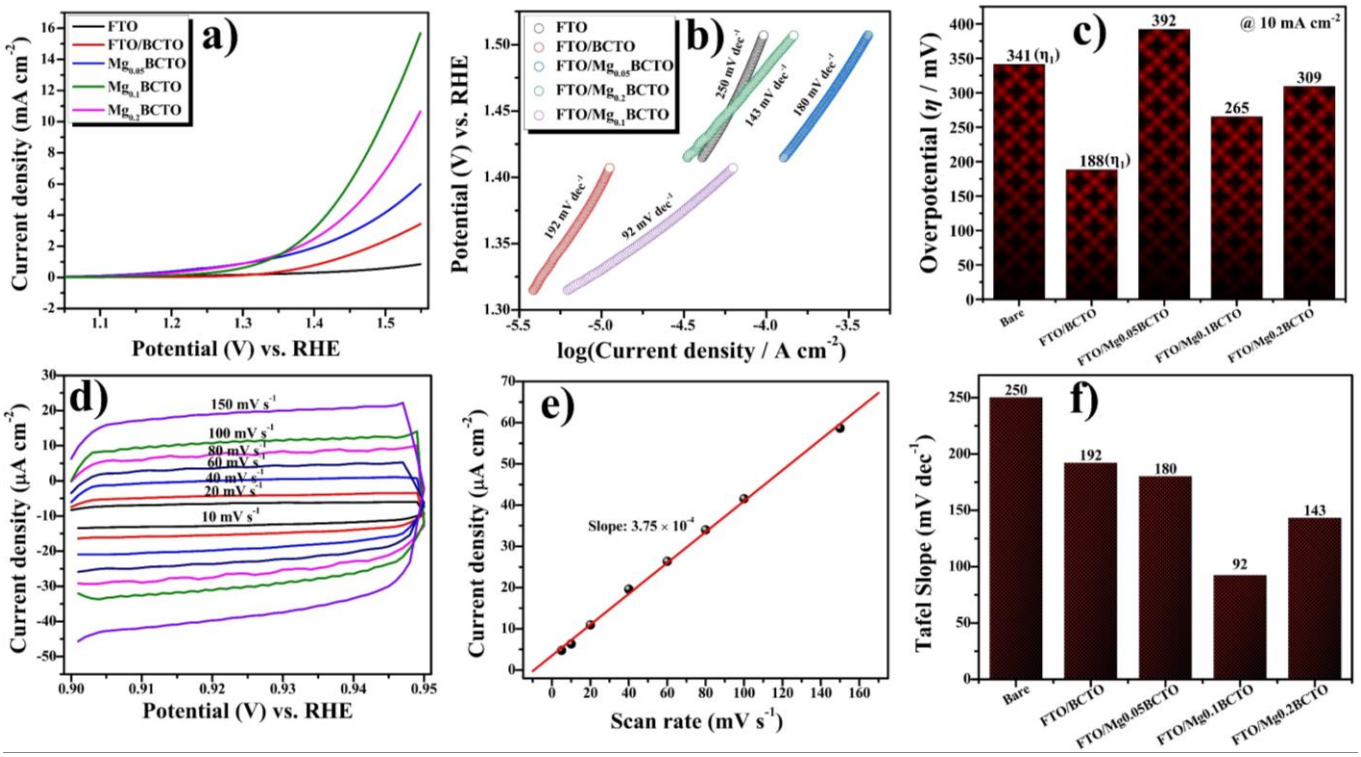

Figure 3.12. a) LSV at a scan rate of 0.5 mV s^{-1} in 1 M KOH at 25 ^{o}C, **b)** Tafel slopes, **c)** Variation of overpotential with as prepared catalysts and bare electrode, **d)** CV of FTO/$Mg_{0.1}$BCTO electrode in non-faradaic region at different scan rates, **e)** Corresponding C_{dl} plot for FTO/$Mg_{0.1}$BCTO electrode **f)** Variation of Tafel slopes with as prepared catalysts and bare electrode.

$$j_{spec} = \frac{j_{app}}{material\ loading} \qquad \textbf{(3.3)}$$

$$j_{true} = \frac{j_{app}}{R_f} \qquad \textbf{(3.4)}$$

Where, R_f is roughness factor.

From the CV, **(Figure 3.13)** the values of three current densities viz. apparent (j_{app}), true (j_{true}), and specific (j_{spec}), in addition to the overpotential values (at specified current

densities), and other kinetic parameters, for the prepared catalysts are provided in **Table 3.1** (calculated from different plots of other catalysts and bare electrode as shown in **Figure 3.17, 3.18, 3.19, and 3.20**). Either the j_{app} or the j_{true}, normalized by the geometric surface area of the electrode or the oxide roughness factor, may be used to indicate the kinetics of electrochemical oxygen evolution.

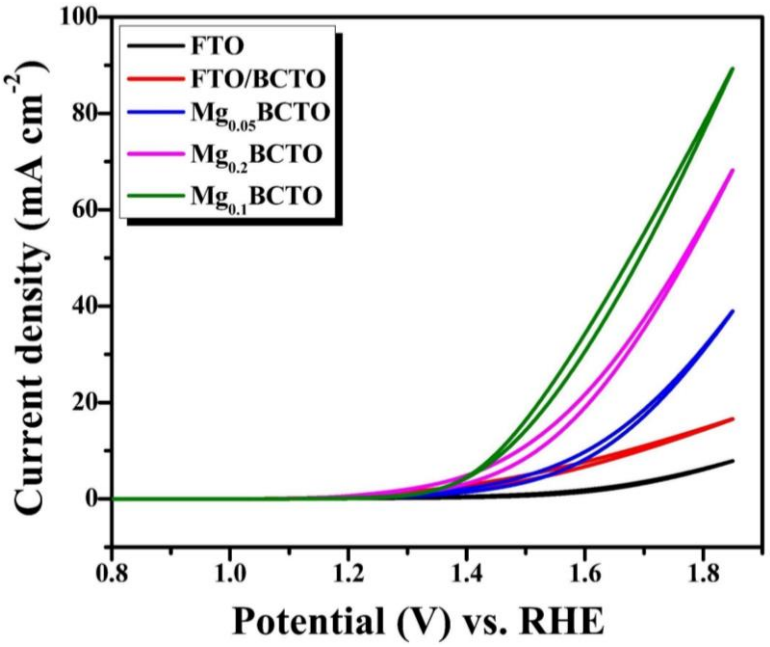

Figure 3.13. CV of prepared catalysts and bare electrode.

The analytical Tafel equation was used to calculate the Tafel slope, which is a measure of catalytic activity ($\eta = b \log j$) [48]. A low Tafel slope value is desirable for efficient electrocatalysts because it indicates faster reaction kinetics. Among the catalysts tested, $Mg_{0.1}$BCTO demonstrated the most favorable catalytic activity, indicated by its significantly lower Tafel slope value of 92 mV dec^{-1} **(Figure 3.12 (b))**, confirming its superior kinetics relative to the other samples **(Figure 3.12 (f))**. The Tafel slopes for the other catalysts and the bare electrode are listed in **Table 3.1** for comparison. This lower Tafel slope and higher current

density for $Mg_{0.1}$BCTO were further validated by Nyquist plots, which showed that, it has the lowest charge transfer resistance among the other stoichiometries studied, underscoring its efficiency as an electrocatalyst.

Table 3.1. Electrode kinetic parameters.

Electrode	**Overpotential (mV) at 10 mA cm^{-2}**	**Current density at E = 1.75 V (mA cm^{-2})**			**C_{dl} (μF cm^{-2})**	**R_f**	**ECSA (cm^2)**	**Tafel Slope (mV dec^{-1})**
		j_{app}	j_{true}	j_{spec}				
Bare	341 (η_1)	4.88	9.38	14.78	20.82	0.52	0.13	250
FTO/BCTO	188 ((η_1)	12.00	12.40	36.36	38.70	0.96	0.24	192
FTO/$Mg_{0.05}$BCTO	392	24.00	15.43	72.72	62.20	1.55	0.38	180
FTO/$Mg_{0.1}$BCTO	**265**	**66.00**	**14.09**	**200.00**	**187.35**	**4.68**	**1.17**	**92**
FTO/$Mg_{0.2}$BCTO	309	46.00	26.74	139.39	68.8	1.72	0.43	143

The double layer capacitance was determined by conducting cyclic voltammetry (CV) in the non-faradaic region (0.90 V – 0.95 V vs. RHE) with scan rates ranging from 20 mV s^{-1} to 150 mV s^{-1} **(Figure 3.12 (d))**. A graph was generated by plotting the scan rate against the current density to get a linear plot **(Figure 3.12 (e))**. The measure of C_{dl} **(Equation 3.5)** could be determined by taking half of the slope of this line [49].

$$C_{dl} = \frac{\Delta j}{2d(V_b)} \quad \textbf{(3.5)}$$

Where, Δj is charging current density,

V_b is scan rate.

The investigation included the calculation of the electrochemically active surface area (ECSA) and roughness factor (R_f) of the catalysts. The R_f value offers valuable information on the arrangement and dispersion of active sites in a system. A value of R_f higher than 1 indicates a larger and more advantageous adsorption region which is calculated from **Equation 1.25** [50]. The ECSA was calculated using the relevant methods **(Equation 1.24),** and it was found that $Mg_{0.1}$BCTO exhibited a higher double layer capacitance (C_{dl}) value of 187.35 μF cm^{-2} and a larger ECSA of 1.17 cm^2 compared to the other catalysts **(Table 3.1)**. A higher ECSA value indicates that the material has a greater number of active sites that are exposed. These active sites play a critical role in facilitating the transfer of electrons and protons between the electrolyte and the electrode, and they also engage in the process of electrolysis [51]. Additionally, The ECSA measurements have been normalized to mass loading of catalysts and the results are shown in **Figure 3.15 (a)**.

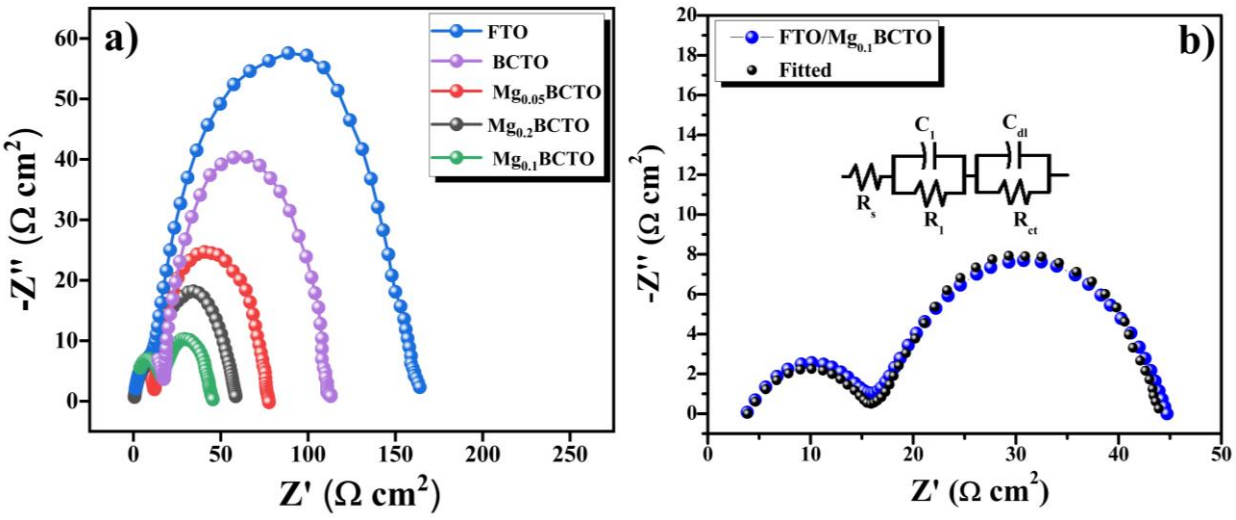

Figure 3.14. a) Nyquist plots, **b)** Fitted Nyquist plot of FTO/$Mg_{0.1}$BCTO electrode.

The rate at which charge is transferred between adsorbed intermediates at the electrode interface was assessed using electrochemical impedance spectroscopy (EIS) [52]. The EIS measurements were performed at 0.90, 1.00, 1.05, 1.15, 1.25 and 1.35 V vs. RHE **(Figure 3.16)** in the frequency range of 100 kHz to 0.01 Hz at 5 mV perturbation amplitude, but reported at onset potential, which is visually represented through Nyquist plots, as illustrated in **Figure 3.14 (a)**. Also, Nyquist plots normalized by mass loading of the catalysts are illustrated in **Figure 3.15 (b)**. In these plots, the appearance of a semicircle on the Z_{real} axis is indicative of charge transfer resistance (R_{ct}). Notably, if the semicircle originates from the origin of Z_{real} axis, it also encompasses the solution resistance [52]. When comparing the Nyquist plots of prepared catalysts, the $Mg_{0.1}$BCTO displayed the smallest semicircle curvature. This suggests that $Mg_{0.1}$BCTO presents the lowest charge transfer resistance during the OER. The reduced resistance is likely due to the optimized ECSA of the $Mg_{0.1}$BCTO, which facilitates a greater accumulation of charge near the electrode surface, thereby enhancing the overall electrochemical performance.

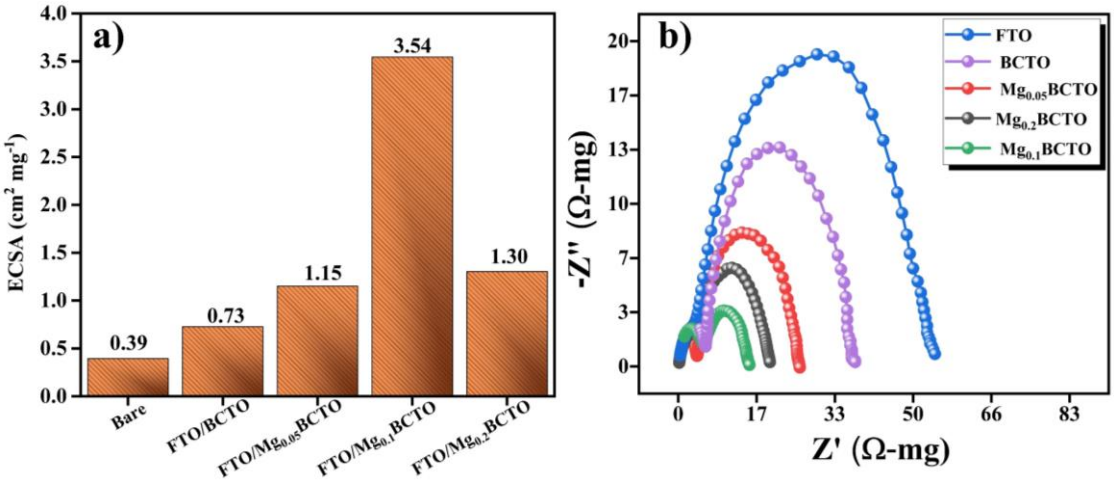

Figure 3.15. a) Comparative ECSA for all the prepared catalysts normalized by mass loading, **b)** Nyquist plots normalized by mass loading of the catalysts.

The semicircles observed in Nyquist plots at different frequency regions represent the adsorption and desorption processes of reactive intermediates (H^+/OH^-) and the charge transfer resistance (R_{ct}). These EIS findings are consistent with the LSV experiments and provide a comprehensive understanding of the catalytic performance of the materials. The analysis of Nyquist plot is based on an equivalent circuit model, depicted in the inset of **Figure 3.14 (b)**. This model includes R_s, representing the solution resistance; R_1, indicating the electrode surface resistance from the catalyst to the electrode surface; and R_{ct}, corresponding to the charge transfer resistance [53,54]. Typically, a lower R_{ct} value indicates a more rapid electron transfer process.

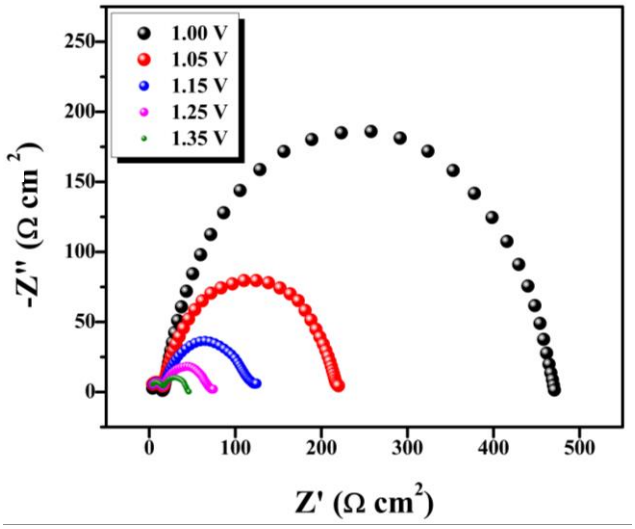

Figure 3.16. Nyquist plots of FTO/$Mg_{0.1}$BCTO electrode on increasing potential.

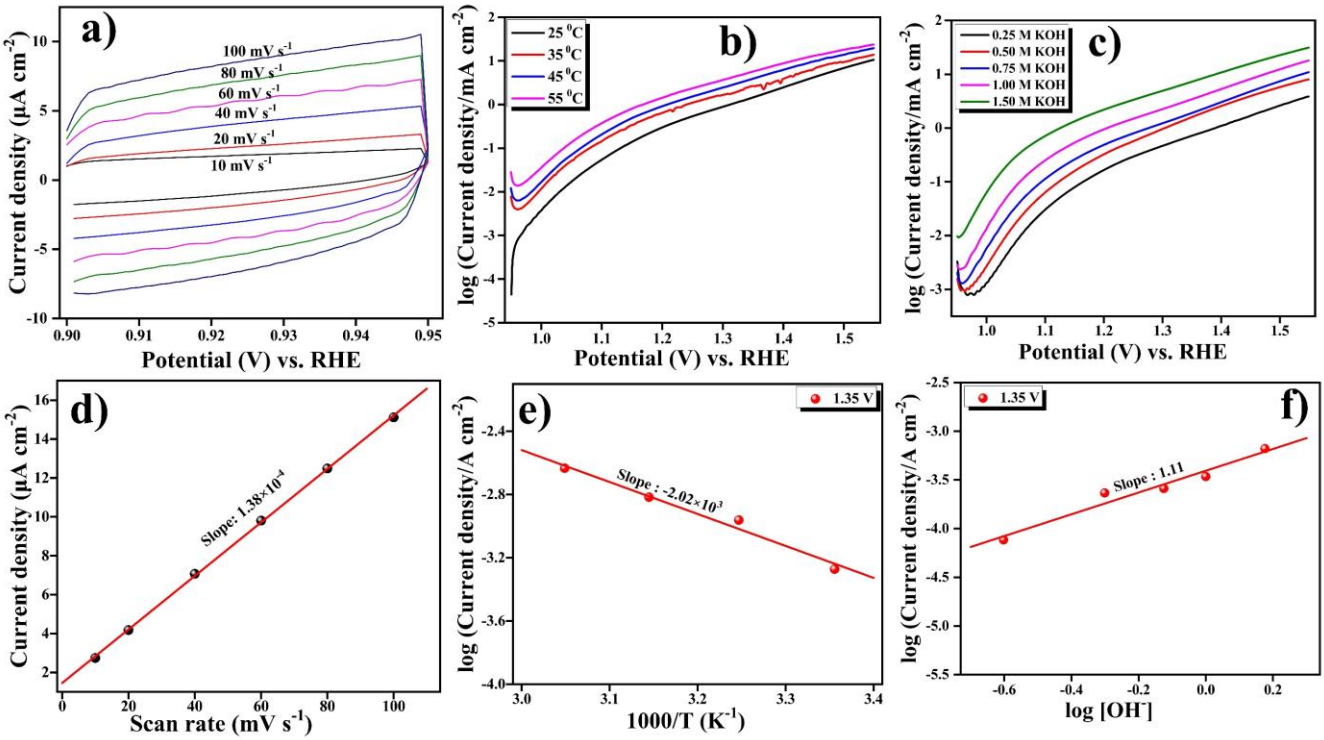

Figure 3.17. a) CV of FTO/$Mg_{0.2}$BCTO electrode in non-faradaic region at different scan rates, **b)** Tafel polarization curves of FTO/$Mg_{0.2}$BCTO electrode at different temperatures, **c)** Tafel polarization curves of FTO/$Mg_{0.2}$BCTO electrode at different concentrations of KOH, **d)** Corresponding C_{dl} plot for FTO/$Mg_{0.2}$BCTO electrode, **e)** Corresponding Arrhenius plot for FTO/$Mg_{0.2}$BCTO, **f)** order of reaction for FTO/$Mg_{0.2}$BCTO electrode.

Analysis of the fitting data reveals that the $Mg_{0.1}$BCTO exhibits the lowest R_{ct} value of 29.57 Ω. In comparison, BCTO, $Mg_{0.05}$BCTO, and $Mg_{0.2}$BCTO show R_{ct} values of 94.40 Ω and 65.20 Ω, and 48.20 Ω respectively. These results demonstrate that the $Mg_{0.1}$BCTO achieves optimal charge transfer efficiency and enhanced catalytic activity

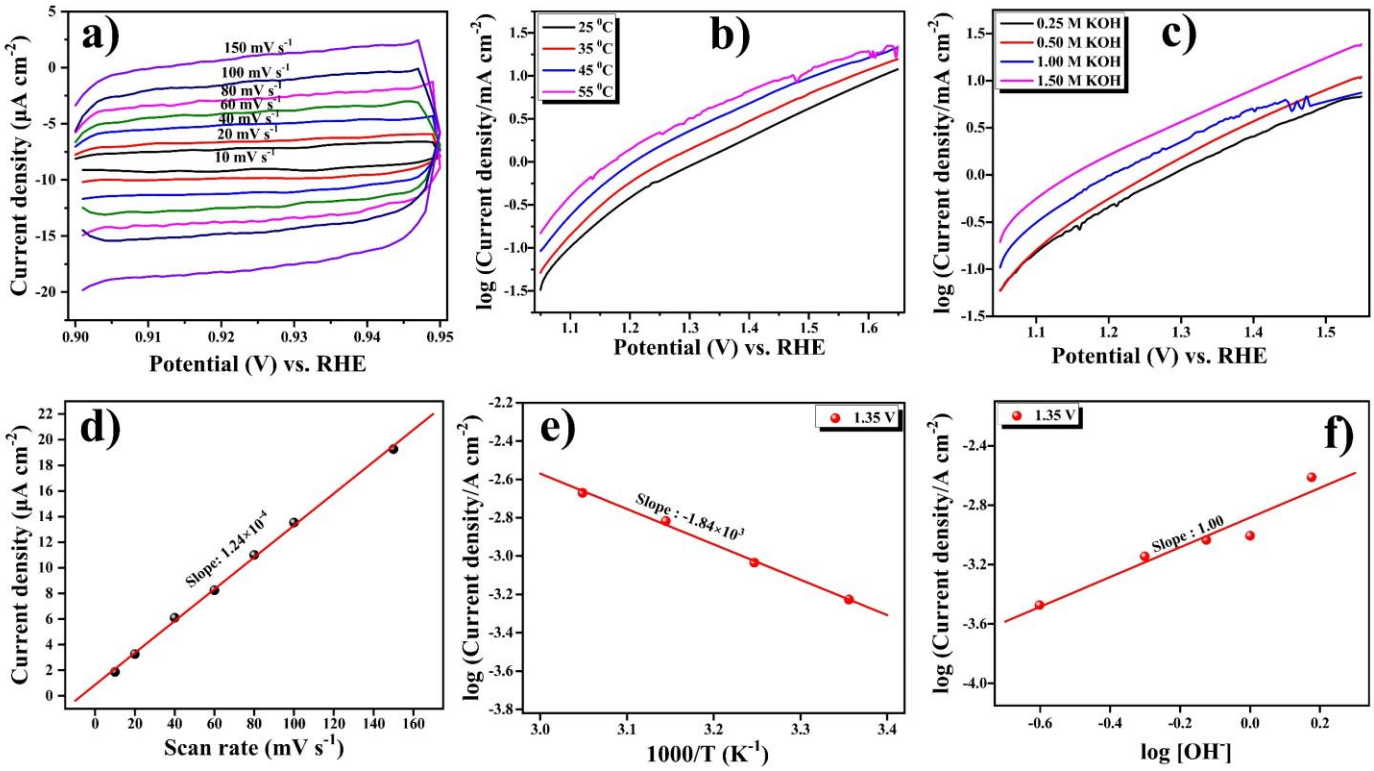

Figure 3.18. a) CV of FTO/$Mg_{0.05}$BCTO electrode in non-faradaic region at different scan rates, **b)** Tafel polarization curves of FTO/$Mg_{0.05}$BCTO electrode at different temperatures, **c)** Tafel polarization curves of FTO/$Mg_{0.05}$BCTO electrode at different concentrations of KOH, **d)** Corresponding C_{dl} plot for FTO/$Mg_{0.05}$BCTO electrode, **e)** Corresponding Arrhenius plot for FTO/$Mg_{0.05}$BCTO electrode, **f)** order of reaction for FTO/$Mg_{0.05}$BCTO electrode.

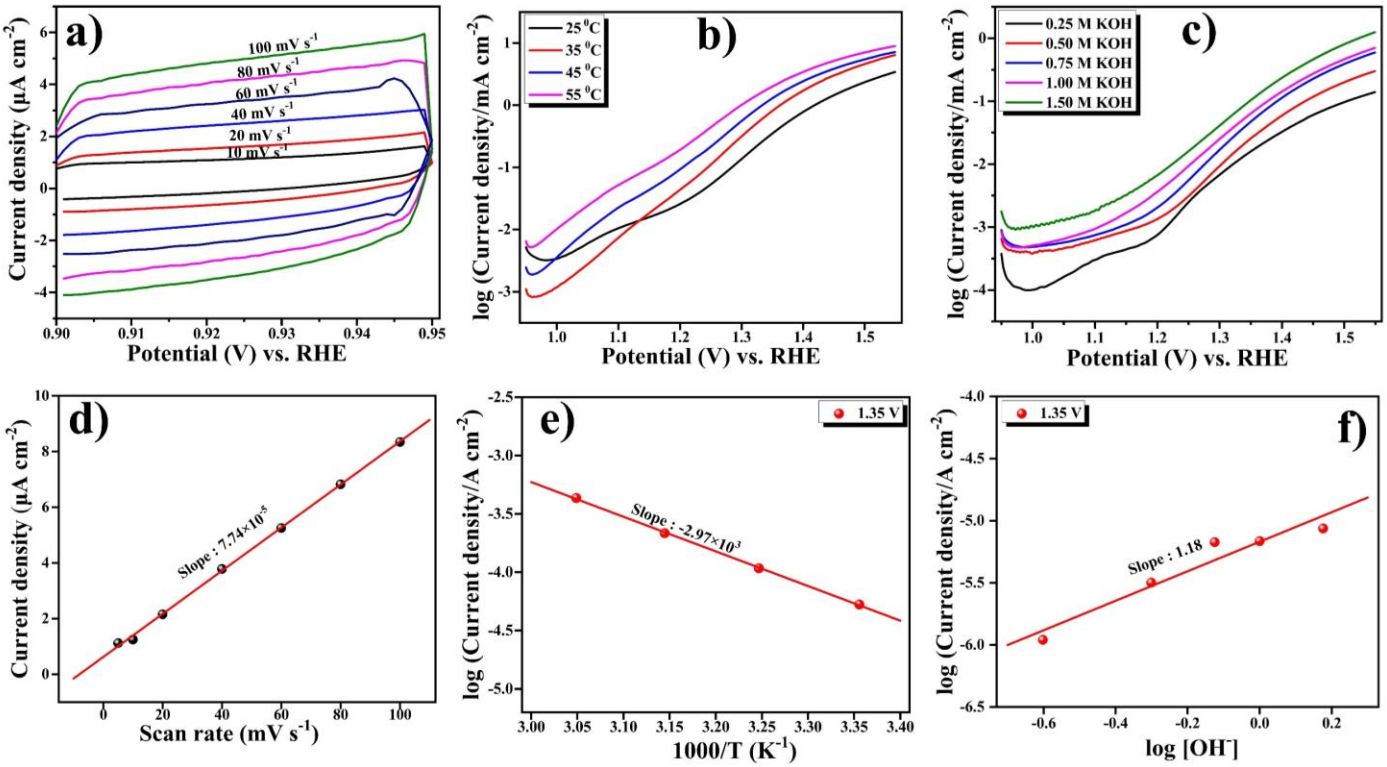

Figure 3.19. a) CV of FTO/BCTO electrode in non-faradaic region at different scan rates, **b)** Tafel polarization curves of FTO/BCTO electrode at different temperatures, **c)** Tafel polarization curves of FTO/BCTO electrode at different concentrations of KOH, **d)** Corresponding C_{dl} plot for FTO/BCTO electrode, **e)** Corresponding Arrhenius plot for FTO/BCTO electrode, **f)** order of reaction for FTO/BCTO electrode.

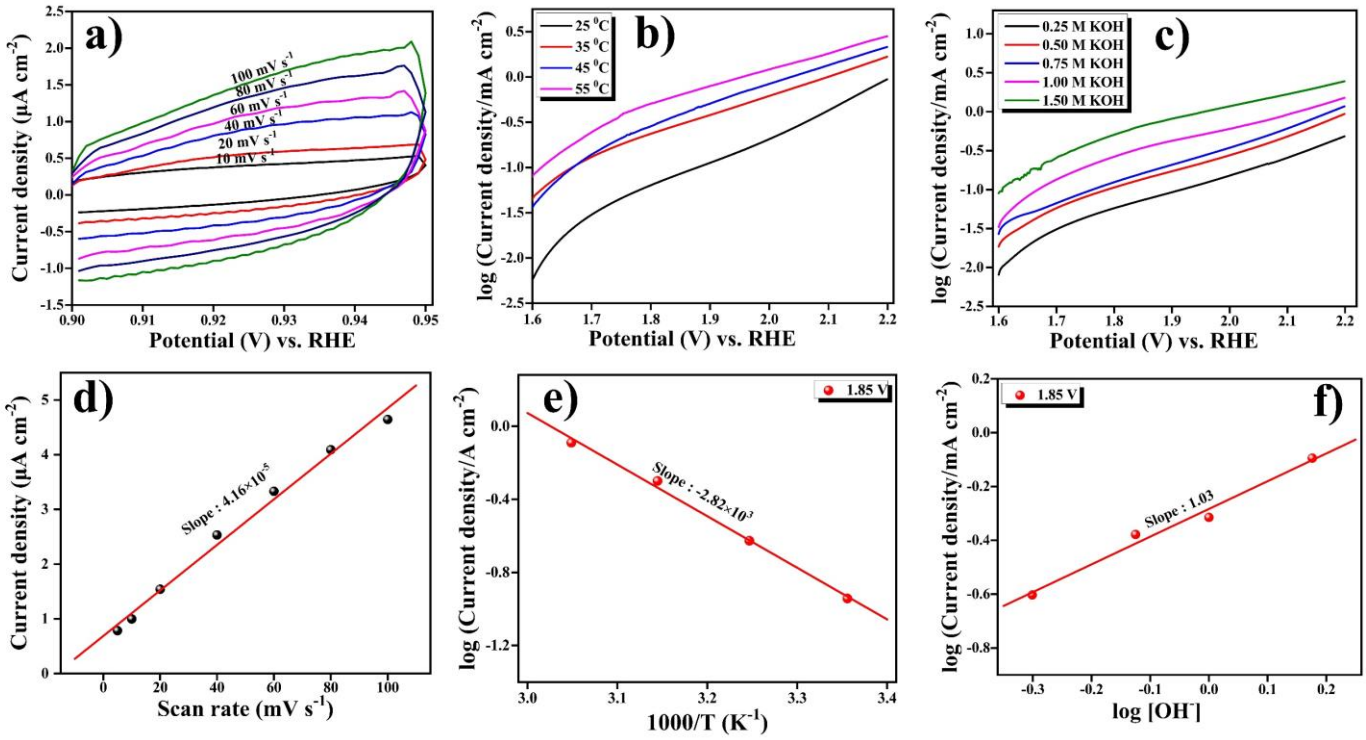

Figure 3.20. a) CV of bare FTO electrode in non-faradaic region at different scan rates, **b)** Tafel polarization curves of bare FTO electrode at different temperatures, **c)** Tafel polarization curves of bare FTO electrode at different concentrations of KOH, **d)** Corresponding C_{dl} plot for bare FTO electrode, **e)** Corresponding Arrhenius plot for bare FTO electrode, **f)** order of reaction for bare FTO electrode.

3.5.2.2. Thermodynamic study

To determine several key thermodynamic parameters such as, the standard electrochemical energy of activation ($\Delta H_{el}^{0\neq}$), the standard entropy of activation ($\Delta S^{0\neq}$), and the standard enthalpy of activation ($\Delta H^{0\neq}$), all the prepared catalysts were investigated. To ensure consistent conditions, the reference electrode was kept at a constant temperature of 25 ^{o}C throughout the experiments. The curves for anodic polarization were recorded in a 1 M KOH solution at temperatures ranging from 25 ^{o}C to 55 ^{o}C. **(Figure 3.21 (a))**. These curves were then used to make corresponding Arrhenius plots, which are depicted in **Figure 3.21 (b)**. The comparative data of thermodynamic parameters for BCTO and Mg doped BCTO are shown in **Table 3.2**. As anticipated, the FTO/$Mg_{0.1}$BCTO electrode demonstrated a lower electrochemical activation energy than the other stoichiometries. This suggests that the $Mg_{0.1}$BCTO material requires less energy to drive the reaction forward, making it more efficient as an electrocatalyst. The transfer coefficient (α) was calculated using the relation $\alpha=2.303RT/bF$, where T is the absolute temperature, F is the Faraday constant, b is tafel slope, and R is the gas constant. For $Mg_{0.1}$BCTO, the average value of α was maximum, indicating efficient electron transfer during the reaction.

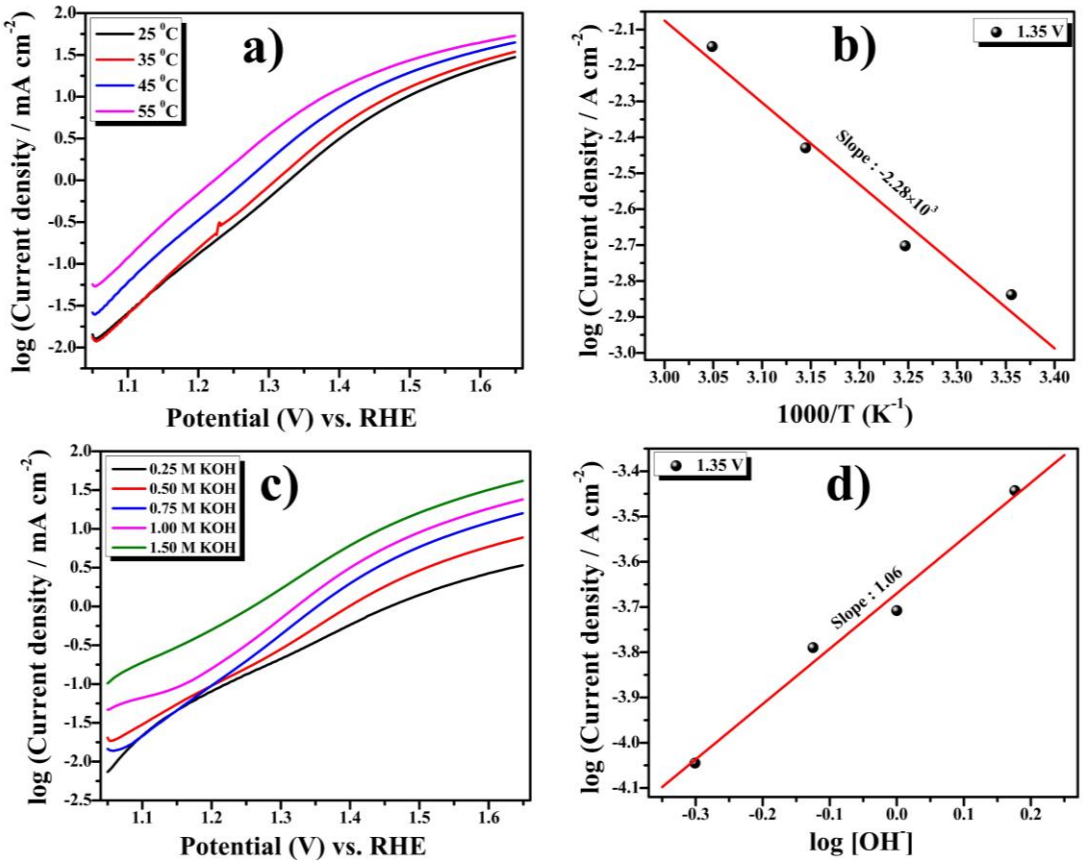

Figure 3.21. a) Tafel polarization curves of FTO/$Mg_{0.1}$BCTO electrode at different temperatures, **b)** Corresponding Arrhenius plot, **c)** Tafel polarization curves of FTO/$Mg_{0.1}$BCTO electrode at different concentrations of KOH **d)** order of reaction.

Further thermodynamic parameters, such as $\Delta S^{0\neq}$ and $\Delta H^{0\neq}$ were determined using **Equations 1.28** and **1.30,** which is already discussed in **Chapter 1.** These parameters provide insights into the energy requirements and the degree of disorder associated with the reaction transition state. Their average values are listed in **Table 3.2**, highlighting the superior performance of the $Mg_{0.1}$BCTO catalyst. The Tafel slope (b), which is derived from the polarization curves obtained at different temperatures, is expressed in mV dec^{-1}. A lower Tafel slope typically indicates better catalytic efficiency and faster reaction kinetics. Finally, the

frequency factor, which includes Planck's constant (h) and the Boltzmann constant (k_B), was calculated as k_BT/h. This factor contributes to understand the frequency of successful collisions between reactants leading to the reaction. Overall, these analyses underscore the enhanced catalytic properties of the FTO/$Mg_{0.1}$BCTO electrode compared to its stoichiometries.

The FTO/$Mg_{0.1}$BCTO electrode exhibits the highest adsorption for the electrochemical generation of oxygen, indicating a greater number of active sites available for the adsorption of reactive species. This is consistent with its most negative $\Delta S^{0\neq}$ value. **Table 3.2** presents detailed thermodynamic values, which can be calculated using the method described in [55].

Table 3.2. Thermodynamic parameters.

Electrode	Standard electrochemical energy of activation ($\Delta H_{el}^{0\neq}$) (kJ mol^{-1})	Standard electrochemical entropy of activation ($-\Delta S_{el}^{0\neq}$) (J $K^{-1}mol^{-1}$)	Transfer coefficient (α)	Standard enthalpy of activation ($\Delta H^{0\neq}$) (kJ mol^{-1})
Bare	58.06	28.72	0.24	104.38
FTO/BCTO	46.52	68.55	0.31	106.35
FTO/$Mg_{0.05}$BCTO	42.14	72.46	0.33	114.83
FTO/$Mg_{0.1}$BCTO	**32.24**	**93.05**	**0.64**	**155.76**
FTO/$Mg_{0.2}$BCTO	37.28	79.08	0.41	116.41

3.5.2.3. Stability and durability

A catalyst has to show remarkable stability in addition to strong catalytic activity in order to be suitable for real-world uses and commercialization. Assessing the long-term stability and durability of an electrocatalyst is crucial to ensure its effectiveness and reliability for practical applications. To assess this aspect, the stability of the FTO/$Mg_{0.1}$BCTO electrode was thoroughly tested through extended chronopotentiometry in a 1 M KOH electrolyte solution. As shown in **Figure 3.22**, the chronopotentiometry results indicated that the electrode continued to have a consistent potential profile even after 12 hours of continuous operation. This observation suggests that the electrode's catalytic activity was not adversely affected by the gas bubbles formed during the process, highlighting its potential in practical applications.

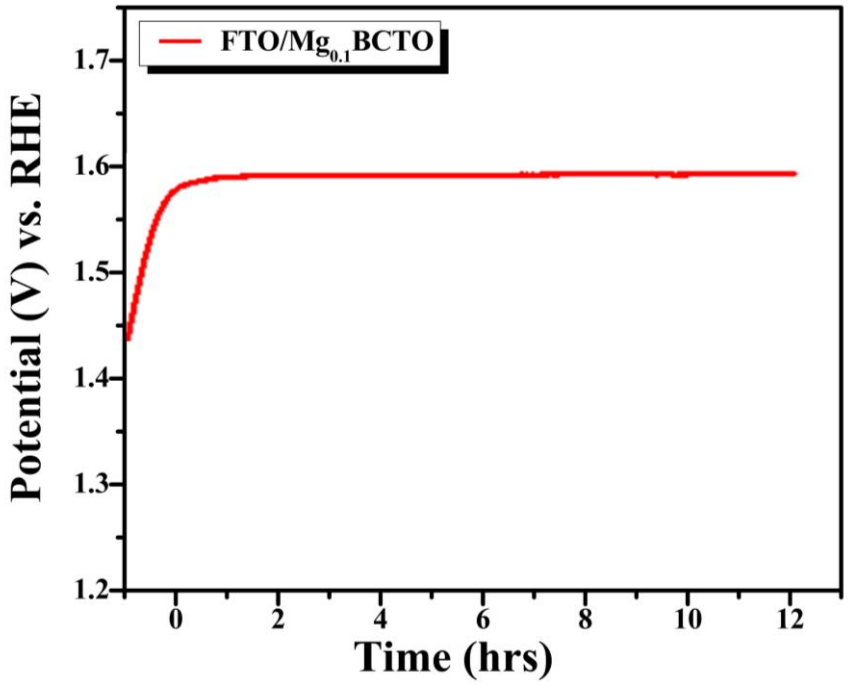

Figure 3.22. Chronopotentiometry test at a constant current of 10 mA cm^{-2}.

3.5.2.4. OER mechanism

For understanding the mechanism of OER, we first calculated the order of reaction for the prepared catalysts using different concentrations of KOH [56]. In this study, the OH^- ion concentration is varied from 0.25 M of KOH to 1.25 M of KOH by maintaining the constant ionic strength to 1.5 using KNO_3 electrolyte. The Tafel polarization curves were recorded at each concentration **(Figure 3.21 (c))** and a graph between log (current density) vs. log [OH^-] was plotted. The curve plotted was found to be a straight line and the slope of this straight line gives the order of reaction as shown in **Figure 3.21 (d)**.

For each catalyst, the values obtained were non-integral, which is not uncommon and has been reported in several studies [57,58]. This phenomenon can be explained by the adsorption and ionization of OH^- on the catalyst surface, where hydroxyl groups are involved [59]. Additionally, the total surface coverage by adsorbed intermediates, such as oxygen-containing species formed during the electrochemical generation of oxygen, contributes to these non-integral values. This occurs under Temkin adsorption conditions, which consider that adsorption energy decreases linearly with increasing coverage, influencing the behavior of the catalysts during the reaction [60,61].

The oxygen evolution reaction (OER) process in alkaline media typically involves four electrochemical steps, including one electron transfer at each step. The process begins at the active sites of the metal (M), where OH^- ions are adsorbed and released. This is followed by the electro-sorption of OH^- ions, as described in **Equation (3.6).** Subsequently, an O-O bond is formed through a series of intermediates, including OH^*, O^*, and OOH^*, which are adsorbed at the metal's active sites, denoted by M-O bonding **(Equations (3.7), (3.8), and (3.9)).** These

chemical steps are well-documented in previous research as part of the OER mechanism [42,48].

$$OH^- + M \rightarrow M + OH^* + e^- \quad \textbf{(3.6)}$$

$$OH^* + OH^- \rightarrow O^* + H_2O + e^- \quad \textbf{(3.7)}$$

$$OH^- + O^* \rightarrow OOH^* + e^- \quad \textbf{(3.8)}$$

$$OH^- + OOH^* \rightarrow O_2 + H_2O + e^- \quad \textbf{(3.9)}$$

This mechanism closely resembles the electrochemical pathway proposed by Bockris [60]. However, it is crucial to acknowledge the potential existence of alternative pathways, such as the Bockris-Otagawa peroxide route and Krasil'shchikov's pathway [60]. According to the proposed mechanism, O^* and OH^* serve as surface-adsorbed intermediates, with 'M' acting as the active site on the surface. This highlights the complexity and versatility of the OER process, where different pathways and intermediates can influence the overall reaction dynamics.

3.6. Conclusion

The catalysts were evaluated for their potential as electrocatalysts to facilitate the oxygen evolution reaction (OER) in an alkaline medium (1 M KOH). The experimental results indicated that BCTO and Mg doped BCTO could be synthesized in a cost-effective and straightforward manner using a semi-wet process. Notably, the FTO/$Mg_{0.1}$BCTO electrode exhibited the lowest Tafel slope, highlighting its superior electrocatalytic activity for OER in an alkaline environment. This catalyst demonstrated nearly first-order kinetics for the OER process, emphasizing its efficiency. Among the tested catalysts, $Mg_{0.1}$BCTO also had the lowest standard electrochemical activation energy, further confirming its effectiveness.

In addition to its application in OER, BCTO and Mg doped BCTO materials show promise to electrode materials for energy conversion and other applications. By utilizing efficient OER catalysts like $Mg_{0.1}$BCTO, large-scale practical water splitting can be achieved, providing the efficient and clean energy required to meet modern energy demands. This advancement holds significant potential for addressing current and future energy challenges by enabling the development of sustainable energy solutions.

3.7. References

[1] T. Abe, M. Kaneko, Reduction catalysis by metal complexes confined in a polymer matrix, Prog. Polym. Sci. 28 (2003) 1441–1488. https://doi.org/10.1016/S0079-6700(03)00057-1.

[2] M. Higashi, K. Domen, R. Abe, Fabrication of an efficient BaTaO2N photoanode harvesting a wide range of visible light for water splitting, J. Am. Chem. Soc. 135 (2013) 10238–10241. https://doi.org/10.1021/ja404030x.

[3] M. Serhan, M. Sprowls, D. Jackemeyer, M. Long, I.D. Perez, W. Maret, N. Tao, E. Forzani, Total iron measurement in human serum with a smartphone, in: AIChE Annu. Meet. Conf. Proc., 2019: pp. 1–3. https://doi.org/10.1039/x0xx00000x.

[4] S. Wang, A. Lu, C.J. Zhong, Hydrogen production from water electrolysis: role of catalysts, Nano Converg. 8 (2021) 1–23. https://doi.org/10.1186/S40580-021-00254-X/FIGURES/16.

[5] S. Shiva Kumar, V. Himabindu, Hydrogen production by PEM water electrolysis – A review, Mater. Sci. Energy Technol. 2 (2019) 442–454. https://doi.org/10.1016/j.mset.2019.03.002.

[6] W.H. Huang, X.M. Li, X.F. Yang, H. Bin Zhang, F. Wang, J. Zhang, Highly efficient electrocatalysts for overall water splitting: mesoporous CoS/MoS2with hetero-interfaces, Chem. Commun. 57 (2021) 4847–4850. https://doi.org/10.1039/d1cc01578h.

[7] G. Zhao, K. Rui, S.X. Dou, W. Sun, Boosting electrochemical water oxidation: The merits of heterostructured electrocatalysts, J. Mater. Chem. A 8 (2020) 6393–6405. https://doi.org/10.1039/d0ta00708k.

[8] Y. Lee, J. Suntivich, K.J. May, E.E. Perry, Y. Shao-Horn, Synthesis and activities of rutile IrO 2 and RuO 2 nanoparticles for oxygen evolution in acid and alkaline solutions, J. Phys. Chem. Lett. 3 (2012) 399–404. https://doi.org/10.1021/JZ2016507/SUPPL_FILE/JZ2016507_SI_001.PDF.

[9] A. Grimaud, K.J. May, C.E. Carlton, Y.L. Lee, M. Risch, W.T. Hong, J. Zhou, Y. Shao-Horn, Double perovskites as a family of highly active catalysts for oxygen evolution in alkaline solution, Nat. Commun. 4 (2013). https://doi.org/10.1038/ncomms3439.

[10] A. Grimaud, O. Diaz-Morales, B. Han, W.T. Hong, Y.L. Lee, L. Giordano, K.A. Stoerzinger, M.T.M. Koper, Y. Shao-Horn, Activating lattice oxygen redox reactions in metal oxides to catalyse oxygen evolution, Nat. Chem. 9 (2017) 457–465. https://doi.org/10.1038/nchem.2695.

[11] J. Hwang, R.R. Rao, L. Giordano, Y. Katayama, Y. Yu, Y. Shao-Horn, Perovskites in catalysis and electrocatalysis, Science (80-.). 358 (2017) 751–756. https://doi.org/10.1126/science.aam7092.

[12] Z.W. She, J. Kibsgaard, C.F. Dickens, I. Chorkendorff, J.K. Nørskov, T.F. Jaramillo, Combining theory and experiment in electrocatalysis: Insights into materials design, Science (80-.). 355 (2017). https://doi.org/10.1126/science.aad4998.

[13] V.S. Rai, S. Pandey, V. Kumar, M.K. Verma, A. Kumar, S. Singh, D. Prajapati, K.D. Mandal, Investigation of microstructure and dielectric behavior of Bi2/3Cu3−xMgxTi4O12 (x = 0, 0.05, 0.1 and 0.2) ceramics synthesized by semi-wet route, J. Mater. Sci. Mater. Electron. 32 (2021) 7671–7680. https://doi.org/10.1007/s10854-021-05483-8.

[14] K. Kawashima, R.A. Márquez, Y.J. Son, C. Guo, R.R. Vaidyula, L.A. Smith, C.E. Chukwuneke, C.B. Mullins, Accurate Potentials of Hg/HgO Electrodes: Practical Parameters for Reporting Alkaline Water Electrolysis Overpotentials, ACS Catal. 13 (2023) 1893–1898. https://doi.org/10.1021/acscatal.2c05655.

[15] R.N. Singh, J.P. Pandey, N.K. Singh, B. Lal, P. Chartier, J.F. Koenig, Sol-gel derived spinel MxCo3-xO4 (M = Ni, Cu; 0≤x≤1) films and oxygen evolution, Electrochim. Acta 45 (2000) 1911–1919. https://doi.org/10.1016/S0013-4686(99)00413-2.

[16] R.N. Singh, J.P. Singh, B. Lal, M.J.K. Thomas, S. Bera, New NiFe2-xCrxO4 spinel films for O2 evolution in alkaline solutions, Electrochim. Acta 51 (2006) 5515–5523. https://doi.org/10.1016/j.electacta.2006.02.028.

[17] A.F.L. Almeida, P.B.A. Fechine, M.P.F. Graça, M.A. Valente, A.S.B. Sombra, Structural and electrical study of CaCu 3Ti 4 O 12 (CCTO) obtained in a new ceramic procedure, J. Mater. Sci. Mater. Electron. 20 (2009) 163–170. https://doi.org/10.1007/s10854-008-9675-4.

[18] L.A.-(No Title), U. 1968, Elements of X-ray Crystallography, Techbooks, c1968, 1968.

[19] L. Fang, M. Shen, Effect of laser fluence on the microstructure and dielectric properties of pulsed laser-deposited CaCu3Ti4O12 thin films, J. Cryst. Growth 310 (2008) 3470–3473. https://doi.org/10.1016/j.jcrysgro.2008.05.011.

[20] V. Kumar, S. Pandey, A. Kumar, M.K. Verma, S. Singh, V.S. Rai, D. Prajapati, T. Das, A. Sharma, C.L. Prajapat, A. Gangwar, K.D. Mandal, Investigation of dielectric, magnetic and impedance spectroscopic properties of CaCu3-XMnXTi4-XMnXO12(X = 0.10) nano-ceramic synthesized through semi-wet route, J. Mater. Res. Technol. 9 (2020) 12936–12945. https://doi.org/10.1016/j.jmrt.2020.09.032.

[21] R. Sankar Ganesh, S.K. Sharma, N. Abinnas, E. Durgadevi, P. Raji, S. Ponnusamy, C. Muthamizhchelvan, Y. Hayakawa, D.Y. Kim, Fabrication of the flexible nanogenerator from BTO nanopowders on graphene coated PMMA substrates by sol-gel method, Mater. Chem. Phys. 192 (2017) 274–281. https://doi.org/10.1016/j.matchemphys.2017.02.002.

[22] R.A. Golda, A. Marikani, D.P. Padiyan, Mechanical synthesis and characterization of Bi4Ti 3O12 nanopowders, Ceram. Int. 37 (2011) 3731–3735. https://doi.org/10.1016/j.ceramint.2011.04.123.

[23] M.H.A. Mhareb, Y. Slimani, Y.S. Alajerami, M.I. Sayyed, E. Lacomme, M.A. Almessiere, Structural and radiation shielding properties of BaTiO3 ceramic with different concentrations of Bismuth and Ytterbium, Ceram. Int. 46 (2020) 28877–28886. https://doi.org/10.1016/j.ceramint.2020.08.055.

[24] S. Jesurani, S. Kanagesan, R. Velmurugan, C. Thirupathi, M. Sivakumar, T. Kalaivani, Nanoparticles of the giant dielectric material, calcium copper titanate from a sol-gel technique, Mater. Lett. 65 (2011) 3305–3308. https://doi.org/10.1016/j.matlet.2011.06.107.

[25] A.F.L. Almeida, R.S. De Oliveira, J.C. Góes, J.M. Sasaki, A.G. Souza Filho, J. Mendes Filho, A.S.B. Sombra, Structural properties of CaCu3Ti4O12 obtained by mechanical alloying, Mater. Sci. Eng. B 96 (2002) 275–283. https://doi.org/10.1016/S0921-5107(02)00379-3.

[26] J. Mohammed, T.T. Carol T., H.Y. Hafeez, B.I. Adamu, Y.S. Wudil, Z.I. Takai, S.K. Godara, A.K. Srivastava, Tuning the dielectric and optical properties of Pr–Co–substituted calcium copper titanate for electronics applications, J. Phys. Chem. Solids 126 (2019) 85–92. https://doi.org/10.1016/j.jpcs.2018.09.034.

[27] T.T. Carol T, J. Mohammed, R. Bhargava, S. Khan, S. Mishra, S.K. Godara, A.K. Srivastava, Crystal structure refinement, optical properties, dielectric response, and impedance spectroscopy of Ni2+-Co2+ substituted bismuth copper titanate (BCTO), Mater. Chem. Phys. 248 (2020) 122933. https://doi.org/10.1016/j.matchemphys.2020.122933.

[28] N. Kolev, R.P. Bontchev, A.J. Jacobson, V.N. Popov, V.G. Hadjiev, A.P. Litvinchuk, M.N. Iliev, Raman spectroscopy of (formula presented), Phys. Rev. B - Condens. Matter Mater. Phys. 66 (2002) 1–4. https://doi.org/10.1103/PhysRevB.66.132102.

[29] C. Mu, Y. Song, H. Wang, X. Wang, Room temperature magnetic and dielectric properties of cobalt doped CaCu3Ti4O12 ceramics, J. Appl. Phys. 117 (2015). https://doi.org/10.1063/1.4916116.

[30] V.S. Rai, D. Prajapati, V. Kumar, M.K. Verma, S. Pandey, T. Das, N.B. Singh, K.D. Mandal, Low temperature synthesis, dielectric and electrical characteristics of Bi2/3Cu3−xNixTi4O12(where x = 0.05, 0.1, and 0.2) ceramics for the dielectric and electrical properties, J. Mater. Sci. Mater. Electron. 33 (2022) 5273–5282. https://doi.org/10.1007/s10854-022-07715-x.

[31] V.S. Rai, D. Prajapati, M.K. Verma, V. Kumar, S. Pandey, T. Das, N.B. Singh, K.D. Mandal, Influence of Zn doping on microstructure, dielectric, and electric properties in Bi2/3Cu3Ti4O12 ceramic synthesized by the semi-wet method, J. Mater. Sci. Mater. Electron. 33 (2022) 14868–14881. https://doi.org/10.1007/s10854-022-08405-4.

[32] N. Imam, G. Aquilanti, A. Azab, S.A.-J. of M. Science, U. 2021, Correlation between structural asymmetry and magnetization in Bi-doped LaFeO3 perovskite: a combined XRD and synchrotron radiation XAS study, SpringerNG Imam, G Aquil. AA Azab, SE AliJournal Mater. Sci. Mater. Electron. 2021•Springer 32 (2021) 3361–3376. https://doi.org/10.1007/s10854-020-05084-x.

[33] F. Khairallah, A. Glisenti, Synthesis, characterization and reactivity study of nanoscale magnesium oxide, J. Mol. Catal. A Chem. 274 (2007) 137–147. https://doi.org/10.1016/j.molcata.2007.04.039.

[34] S.M. Thalluri, S. Hernández, S. Bensaid, G. Saracco, N. Russo, Green-synthesized W- and Mo-doped BiVO4 oriented along the {040} facet with enhanced activity for the sun-driven water oxidation, Appl. Catal. B Environ. 180 (2016) 630–636. https://doi.org/10.1016/j.apcatb.2015.07.029.

[35] Z. Pei, K. Leng, W. Xia, Y. Lu, H. Wu, X. Zhu, Structural characterization, dielectric, magnetic and optical properties of double perovskite Bi2FeMnO6 ceramics, J. Magn. Magn. Mater. 508 (2020) 166891. https://doi.org/10.1016/j.jmmm.2020.166891.

[36] S. Poulston, P.M. Parlett, P. Stone, M. Bowker, Surface oxidation and reduction of CuO and Cu2O studied using XPS and XAES, Surf. Interface Anal. 24 (1996) 811–820. https://doi.org/10.1002/(SICI)1096-9918(199611)24:12<811::AID-SIA191>3.0.CO;2-Z.

[37] H. Qiu, S. Zhang, B. Pan, W. Zhang, L. Lv, Effect of sulfate on Cu(II) sorption to polymer-supported nano-iron oxides: Behavior and XPS study, J. Colloid Interface Sci. 366 (2012) 37–43. https://doi.org/10.1016/j.jcis.2011.09.070.

[38] R. Sanjinés, H. Tang, H. Berger, F. Gozzo, G. Margaritondo, F. Lévy, Electronic structure of anatase TiO2 oxide, J. Appl. Phys. 75 (1994) 2945–2951. https://doi.org/10.1063/1.356190.

[39] N. Drnovšek, N. Daneu, A. Rečnik, M. Mazaj, J. Kovač, S. Novak, Hydrothermal synthesis of a nanocrystalline anatase layer on Ti6A4V implants, Surf. Coatings Technol. 203 (2009) 1462–1468. https://doi.org/10.1016/j.surfcoat.2008.11.031.

[40] X. Li, Y. Wang, W. Liu, G. Jiang, C. Zhu, Study of oxygen vacancies′ influence on the lattice parameter in ZnO thin film, Mater. Lett. 85 (2012) 25–28. https://doi.org/10.1016/j.matlet.2012.06.107.

[41] J.C.C. Fan, J.B. Goodenough, X-ray photoemission spectroscopy studies of Sn-doped indium-oxide films, J. Appl. Phys. 48 (1977) 3524–3531. https://doi.org/10.1063/1.324149.

[42] S. Pal, U.P. Azad, A.K. Singh, D. Kumar, R. Prakash, Studies on some spinel oxides based electrocatalysts for oxygen evolution and capacitive applications, Electrochim. Acta 320 (2019). https://doi.org/10.1016/j.electacta.2019.134584.

[43] R. Xue, L. Zhao, X. Liu, H. Wang, X. Zhu, Y. Xiao, C. Yuan, B. Cao, Z. Chen, T. Li, H. Dai, Enhanced optical, dielectric, and non-Ohmic properties in Ta-doped Bi2/3Cu3Ti4O12 ceramics, Solid State Sci. 150 (2024) 107495. https://doi.org/10.1016/j.solidstatesciences.2024.107495.

[44] S. Peng, F. Gong, L. Li, D. Yu, D. Ji, T. Zhang, Z. Hu, Z. Zhang, S. Chou, Y. Du, S. Ramakrishna, Necklace-like Multishelled Hollow Spinel Oxides with Oxygen Vacancies for Efficient Water Electrolysis, J. Am. Chem. Soc. 140 (2018) 13644–13653. https://doi.org/10.1021/jacs.8b05134.

[45] H. Li, S. Sun, S. Xi, Y. Chen, T. Wang, Y. Du, M. Sherburne, J.W. Ager, A.C. Fisher, Z.J. Xu, Metal-Oxygen Hybridization Determined Activity in Spinel-Based Oxygen Evolution Catalysts: A Case Study of ZnFe2- xCrxO4, Chem. Mater. 30 (2018) 6839–6848. https://doi.org/10.1021/acs.chemmater.8b02871.

[46] H. Zhu, P. Zhang, S. Dai, Recent Advances of Lanthanum-Based Perovskite Oxides for Catalysis, ACS Catal. 5 (2015) 6370–6385. https://doi.org/10.1021/acscatal.5b01667.

[47] A.S. Chaddha, N.K. Singh, M. Malviya, A. Sharma, Birnessite-clay mineral couple in the rock varnish: a nature's electrocatalyst, Sustain. Energy Fuels 6 (2022) 2553–2569. https://doi.org/10.1039/d2se00185c.

[48] Z. Hu, L. Hao, F. Quan, R. Guo, Recent developments of Co3O4-based materials as catalysts for the oxygen evolution reaction, Catal. Sci. Technol. 12 (2022) 436–461. https://doi.org/10.1039/d1cy01688a.

[49] U.J. Awan, M.A. Basit, S.I.A. Shah, J. Yong-Xin, H. Zhifu, Minimized OER overpotential via SILAR-based development of g-C3N4/CdS nanocomposite, Appl. Phys. A Mater. Sci. Process. 129 (2023) 1–15. https://doi.org/10.1007/s00339-023-07105-y.

[50] A. Hojatshamami, Ni-Co and Ni-Fe Catalysts for The Oxygen Evolution Reaction in Alkaline Water Electrolysis, (2022). https://hdl.handle.net/11250/3042808 (accessed June 23, 2024).

[51] H. Zeng, Y. Zeng, J. Qi, L. Gu, E. Hong, R. Si, C. Yang, The role of proton dynamics on the catalyst-electrolyte interface in the oxygen evolution reaction, Chinese J. Catal. 43 (2022) 139–147. https://doi.org/10.1016/S1872-2067(21)63909-8.

[52] A. Bard, L. Faulkner, H. White, Electrochemical methods: fundamentals and applications, 2022. https://books.google.com/books?hl=en&lr=&id=Sct6EAAAQBAJ&oi=fnd&pg=PR21&ots=QV3mtaJ0NX&sig=DLfrR_jFcE_cWnGqn5_EbKOHFu0 (accessed May 6, 2024).

[53] W. Choi, H.C. Shin, J.M. Kim, J.Y. Choi, W.S. Yoon, Modeling and applications of electrochemical impedance spectroscopy (Eis) for lithium-ion batteries, J. Electrochem. Sci. Technol. 11 (2020) 1–13. https://doi.org/10.33961/jecst.2019.00528.

[54] A. Wieczorek, Y. Liu, H.H. Cho, K. Sivula, Assessing the Charge Carrier Dynamics at Hybrid Interfaces of Organic Photoanodes for Solar Fuels, J. Phys. Chem. Lett. 15 (2024) 6347–6354. https://doi.org/10.1021/acs.jpclett.4c01170.

[55] A.S. Chaddha, N.K. Singh, M. Malviya, A. Sharma, Birnessite-clay mineral couple in the rock varnish: a nature's electrocatalyst, Sustain. Energy Fuels 6 (2022) 2553–2569. https://doi.org/10.1039/D2SE00185C.

[56] R.N. Singh, N.K. Singh, J.P. Singh, Electrocatalytic properties of new active ternary ferrite film anodes for O2 evolution in alkaline medium, Electrochim. Acta 47 (2002) 3873–3879. https://doi.org/10.1016/S0013-4686(02)00354-7.

[57] F. Švegl, B. Orel, I. Grabec-Švegl, V. Kaučič, Characterization of spinel Co3O4 and Li-doped Co3O4 thin film electrocatalysts prepared by the sol-gel route, Electrochim. Acta 45 (2000) 4359–4371. https://doi.org/10.1016/S0013-4686(00)00543-0.

[58] R.N. Singh, J.F. Koenig, G. Poillerat, P. Chartier, Thin films of CO3O4 and NiCo2O4 prepared by the method of chemical spray pyrolysis for electrocatalysis. Part IV. The electrocatalysis of oxygen reduction, J. Electroanal. Chem. 314 (1991) 241–257. https://doi.org/10.1016/0022-0728(91)85440-Z.

[59] L.I. Krishtalik, Kinetics and mechanism of anodic chlorine and oxygen evolution reactions on transition metal oxide electrodes, Electrochim. Acta 26 (1981) 329–337. https://doi.org/10.1016/0013-4686(81)85019-0.

[60] J.O.M. Bockris, T. Otagawa, Mechanism of oxygen evolution on perovskites, J. Phys. Chem. 87 (1983) 2960–2971. https://doi.org/10.1021/j100238a048.

[61] R.N. Singh, J.F. Koenig, G. Poillerat, P. Chartier, Thin films of CO3O4 and NiCo2O4 prepared by the method of chemical spray pyrolysis for electrocatalysis. Part IV. The electrocatalysis of oxygen reduction, J. Electroanal. Chem. 314 (1991) 241–257. https://doi.org/10.1016/0022-0728(91)85440-Z.